

Unsteady aerodynamics and flow control for flapping wing flyers

Steven Ho^{a,*}, Hany Nassef^a, Nick Pornsinsirak^b, Yu-Chong Tai^b,
Chih-Ming Ho^a

^a *Department of Mechanical Engineering, University of California, Los Angeles, 38-137J Engineering IV, 420 Westwood Plaza, Los Angeles, CA 90095, USA*

^b *Department of Electrical Engineering, California Institute of Technology, MS 136-93 Caltech, Moore Laboratory, Pasadena, CA 91125 USA*

Abstract

The creation of micro air vehicles (MAVs) of the same general sizes and weight as natural fliers has spawned renewed interest in flapping wing flight. With a wingspan of approximately 15 cm and a flight speed of a few meters per second, MAVs experience the same low Reynolds number (10^4 – 10^5) flight conditions as their biological counterparts. In this flow regime, rigid fixed wings drop dramatically in aerodynamic performance while flexible flapping wings gain efficacy and are the preferred propulsion method for small natural fliers. Researchers have long realized that steady-state aerodynamics does not properly capture the physical phenomena or forces present in flapping flight at this scale. Hence, unsteady flow mechanisms must dominate this regime. Furthermore, due to the low flight speeds, any disturbance such as gusts or wind will dramatically change the aerodynamic conditions around the MAV. In response, a suitable feedback control system and actuation technology must be developed so that the wing can maintain its aerodynamic efficiency in this extremely dynamic situation; one where the unsteady separated flow field and wing structure are tightly coupled and interact nonlinearly. For instance, birds and bats control their flexible wings with muscle tissue to successfully deal with rapid changes in the flow environment. Drawing from their example, perhaps MAVs can use lightweight actuators in conjunction with adaptive feedback control to shape the wing and achieve active flow control. This article first reviews the scaling laws and unsteady flow regime constraining both biological and man-made fliers. Then a summary of vortex dominated unsteady aerodynamics follows. Next, aeroelastic coupling and its effect on lift and thrust are discussed. Afterwards, flow control strategies found in nature and devised by man to deal with separated flows are examined. Recent work is also presented in using microelectromechanical systems (MEMS) actuators and angular speed variation to achieve active flow control for MAVs. Finally, an explanation for aerodynamic gains seen in flexible versus rigid membrane wings, derived from an unsteady three-dimensional computational fluid dynamics model with an integrated distributed control algorithm, is presented.

© 2003 Elsevier Ltd. All rights reserved.

Contents

1. Introduction	636
2. Scaling and geometric similarity	639

*Corresponding author. Defense Advanced Research Projects Agency, 3701 North Fairfax Drive, Arlington, VA 22203-1714, USA.
E-mail address: sho@darpa.mil (S. Ho).

2.1. Wing loading	639
2.2. MAV size and weight	641
2.3. Size and steady versus unsteady flow regimes	641
3. Vortex dominated unsteady aerodynamics	642
3.1. The clap and fling mechanism	643
3.2. Theory of the wake	643
3.3. Rotational lift and wake capture	644
3.4. The unsteady leading edge vortex	645
3.4.1. Unsteady leading edge vortex lift and thrust production	647
4. Aeroelastic coupling and its importance	649
4.1. Aeroelastic models	649
4.2. Flexible and rigid wing lift and thrust production	650
5. Open loop control of separated flows	652
5.1. Natural flier techniques	653
5.2. Delta wing vortex control	653
5.3. Dynamic stall vortex control	654
5.4. Flutter	654
5.4.1. Distributed piezoelectric actuators for flutter control	655
5.5. MEMS for aerodynamic flow control	655
5.6. MEMS electrostatic check-valve actuators	656
6. Active flow control techniques and flapping flight	658
6.1. Closed loop control of separated flows	658
6.2. Linear quadratic (LQ) controllers for flutter suppression	658
6.3. Other linear controllers	659
6.4. Proportional integral derivative control of separated flows	659
6.5. Genetic algorithm optimization	659
6.6. Neural network control of separated flow	659
6.7. Angular speed control	660
6.7.1. Experimental setup	661
6.7.2. Gur Game feedback control	662
6.7.3. Open loop test results	663
6.7.4. Closed loop test results	664
7. Computational fluid dynamics model with integrated feedback control	665
7.1. Flapping wing model description	665
7.1.1. Model validation	666
7.2. Integrated distributed control algorithm model	669
7.3. Physical mechanisms	670
7.4. Mechanical power	675
7.5. Summary of the simulation project	677
8. Concluding remarks	677
Acknowledgements	678
References	678

1. Introduction

Flapping wing flight stands out as one of the most complex yet widespread modes of transportation found in nature. Over a million different species of insects fly with flapping wings, and 10,000 types of birds and bats flap their wings for locomotion [1]. This proliferation of flying species has also attracted scientific attention.

Biologists and naturalists have produced kinematic descriptions of flapping wing motion and empirical correlations between flapping frequency, weight, wingspan, and power requirements based on studies of many different families of birds and insects [2–6]. Biofluid dynamicists have attempted to explain the underlying physical phenomena both in the quasi-steady limit [7,8] and in the fully unsteady regime [9–13]. The quasi-steady

limit mainly corresponds to large birds such as eagles and osprey, which soar and glide. When soaring, the wings are fixed and rigid and act like those of conventional aircraft. For these fliers, flapping is restricted to limited operations, such as take-off, landing, and stabilization. Smaller birds and insects that continuously flap occupy the other end of the aerodynamic spectrum, that of fully unsteady flight. Empirical correlations predict the break between quasi-steady and unsteady flight at approximately 15 cm in wingspan. A 15 cm wingspan is also the arbitrary design limit set for micro air vehicles (MAVs). In fact, desired MAV performance requirements derive from those attributes seen in small birds and insects, namely high maneuverability, very low speed flight capability, and high power and aerodynamic efficiency. It is clear then that any MAV design must account for the same environment as those for similarly sized biological fliers; one where the flow field is unsteady, laminar, incompressible and occurs at low Reynolds number (10^4 – 10^5).

Motivation for this article stems from recent interest in very small payload carrying flight vehicles. Such vehicles would be useful for remote sensing missions where access is restricted due to various hazards. These vehicles have a typical wingspan of 15 cm, with a weight restriction of less than 100 g [14]. The goal is to consider a flapping wing design and adaptive flow control as a novel approach to the problem, since the size and speed range of the vehicle closely matches that of small birds and insects, which are obviously very capable fliers. The most striking feature of bird and insect flight is of course the cyclic flapping motion of the wings that generates sufficient lift and thrust to support the body in forward or hovering flight. Large amplitude motion and periodic acceleration and deceleration of the wings lead to large inertial forces, significant unsteady effects, and gross departures from standard linear aerodynamic and aeroelastic theory. For example, birds and bats operate in the $10^4 < Re < 10^6$ domain, a regime where the flow field is very sensitive to slight changes that could either promote or inhibit separation and the transition to turbulence [15]. Hence, the performance of their wings could fluctuate accordingly. Certainly, the exact wing kinematics wields great influence over the resulting flow field and many researchers have captured and mapped bird wing motion with high-speed video cameras [16–18]. Insects, birds, and bats were found to produce complex motions that can consist of flexing, twisting, bending, rotating, or feathering their wings throughout the entire flapping cycle. Comprehensive reviews of wing kinematics and biological flight evolution can be found in Rayner [19,20], Norberg [21], and Pennycuik [22]. Readers interested in the power requirements for flapping and hovering flight for insects and birds are referred to Azuma et al. [23], Azuma and Watanabe [24],

Wakeling and Ellington [25–27], Van den Berg and Rayner [28], and Rayner [29,30].

It has long been realized that steady-state aerodynamics does not accurately account for the forces produced by natural fliers, and this has prompted several studies [31–33] on the unsteady flow produced. Spedding gives an excellent review of the early aerodynamic models of flapping flight (momentum jet, blade element analysis, vortex wake models, hybrid blade element and vortex models, and unsteady lifting line methods). Mechanisms such as rotational circulation, wake capture, and the unsteady leading edge vortex do seem to properly account for the aerodynamics forces. Regarding forward flight, the unsteady leading edge vortex is the only mechanism present to produce the necessary forces. The unsteady leading edge vortex involves leading edge flow separation that reattaches to the wing and forms a separation bubble. The vortex increases the circulation around the wing and creates much higher lift than the steady-state case. This vortex remains stable due to its highly three-dimensional nature [34].

These unsteady forces combine with the thin and flexible wing structure to produce large amplitude wing deformations, which interact nonlinearly with the flow field. For example, bats can control their wing surface by changing the degree of tension in their wing membrane, thereby effectively changing the wing camber due to the passive aeroelastic response of the membrane to the aerodynamic loading. Birds and bats also twist and bend their wings for optimal lift and thrust while maneuvering. Clearly, wing stiffness distribution and flexibility are important aspects when considering natural fliers. This is also true of artificial fliers. Smith [35] commented on the importance of flexibility and wing stiffness in accurately modeling the flapping motion and the resultant force generation. Shyy et al. [36,37] conducted a systematic numerical study of adaptive airfoils in response to oscillatory flows and found that passive airfoils that deform in accordance with the local pressure distribution can increase the lift coefficient significantly.

Alongside experimental work investigating biological wings in unsteady flows, there have been several studies using computational fluid dynamics (CFD) techniques to validate different aerodynamic models and to illuminate the phenomena underlying flapping flight. Among the first simulations were conducted by Smith [35]. He computed the 3-D unsteady flow field around a tethered moth wing and emphasized the importance of including the effect of the wake in the analysis. Separate groups [38,39] also simulated insect flight and examined the importance of wing rotation at the end of the stroke length. These groups reported relatively good agreement between the numerical results and experimental data taken from an oil tank model. A 2-D model by

Wang [40] investigated vortex shedding and found an optimal flapping frequency based on time scales associated with shedding of the leading and trailing edge vortices. Finally, Liu et al. [41] demonstrated the existence and stability of the unsteady leading edge vortex on a simulation of the hawkmoth wing. These computations all show that the generation and shedding of vortices dominate the aerodynamic loading on the wing. The periodicity of the wing motion and the resultant vortices leads to the conclusion that any quantitative model must be based on unsteady aerodynamics and vortex dynamics.

Furthermore, the field of flow control strategies to increase lift and thrust for mechanical flapping flight remains a relatively unexplored arena. Previous studies exist on natural fliers and their methods of increasing lift, but there is a dearth of research for artificial fliers. Yet the unsteady flow field and the tight aeroelastic coupling between the wing deformation and the surrounding fluid offers great hope that small actuators placed at the right position, and combined with an appropriate feedback controller, could lead to large gains in aerodynamic performance with relatively modest power inputs. The main challenges involved would then be in fabricating the actuators in line with the weight constraints and selecting the appropriate feedback controller for such a highly nonlinear system.

Finally, the physical system under consideration, where flow separation occurs in the presence of a very flexible and deformable airfoil, is an exceedingly difficult analytic problem. It is a highly nonlinear system—the flow field is fully unsteady and three dimensional, with important near field viscous effects and a close dynamic coupling between the fluid and the airfoil structure. This type of environment falls far outside the operational envelope of conventional aircraft, where steady and smoothly attached flow is the norm. The need to investigate and optimally control this system grows, however, with the advent of MAVs and small unmanned air vehicles (UAVs). These aircraft will routinely experience these conditions as operational requirements call for low speed forward flight combined with supermaneuverability. A further complication is the requirement of an efficient and low-power actuation system that does not compromise the air vehicle's observability. It is possible that a control and actuation system developed for this system will also be applicable to more conventional aerodynamic problems, such as the control of flutter or the dynamic stall vortex (DSV) found on helicopter rotor blades.

This review attempts to tie together phenomenological descriptions of unsteady flapping flight, past experimental and numerical work in modeling flapping wings, unsteady flow control methodologies used in nature and by man, and presents some new experiments undertaken in adaptive unsteady flow control for flexible wings.

By focusing on unsteady flow fields and its control, we hope to highlight the dominant physical phenomena and point toward new paths that aerodynamicists can explore in the design of future MAVs.

The following topics are covered in this review:

Section 2 summarizes the concepts of geometric similarity and scaling laws with consideration for both biological and artificial fliers. Particular attention is paid to determining which flow regime (quasi-steady or unsteady) MAVs fall into and how they compare with small birds in terms of weight and flight speed. Simple empirical correlations for flapping frequency versus wing length and flapping frequency versus mass are combined to generate a plot of flow unsteadiness as a function of body mass.

Section 3 briefly reviews previous models of unsteady aerodynamics in insect and bird flight from a variety of researchers. Models covered are the 'clap and fling' mechanism, the theory of the wake, rotational lift and wake capture, and the unsteady leading edge vortex. The main lesson is that slow speed forward flapping flight or hovering flight depends on vortex dominated unsteady aerodynamics. These vortices and their interaction with the wing during the flapping cycle drives the lift and thrust production.

Section 4 emphasizes the role of aeroelastic coupling between the wing and surrounding fluid and its relation to lift and thrust performance. Most previous analysis of flapping flight (both numerical and analytic) assumed a rigid wing and no fluid–structure interaction. This assumption, however, is not applicable to natural fliers, which have very light and flexible wings that certainly deform aeroelastically. This realization is applied to MAVs and experimental data clearly demonstrates how wing stiffness and flexibility affect lift and thrust production.

Section 5 shifts the discussion to flow control and its application to flapping flight. Instances of open loop flow control strategies employed in nature are given, as are examples of open and closed loop flow control of separated flows. These include dynamic stall control on rotorcraft, leading edge suction and blowing on delta wings, and the use of adaptive control algorithms such as neural networks and genetic algorithms. Due to weight and power constraints as well as the extremely large nonlinear problem space, these actuation schemes and control algorithms do not seem suitable for flapping flight control. Instead, new methods using microelectromechanical system (MEMS) actuators are investigated.

Section 6 presents an adaptive closed loop control system for separated flow over a highly deformable wing embedded with distributed MEMS actuators. Control is achieved with the Gur Game algorithm, in which simple finite state automata optimize the behavior of individual actuators based on the performance of the actuator set

as a whole. Finally, the details of the Gur Game algorithm and an experimental investigation are detailed.

Section 7 describes an unsteady three-dimensional CFD model of the flapping wing coupled with a finite element model (FEM) of the wing that fully captures the strong aeroelastic interaction of the fluid field and the wing structure. Additionally, a distributed control and optimization algorithm is integrated with the simulation model. This model is used to optimize the wing and the physical mechanisms underlying the improvements in aerodynamic performance are illustrated.

2. Scaling and geometric similarity

Based on the concept of geometric similarity, scaling laws derived from regression analysis of whole species and families of birds, bats, and insects will aid in determining what range of sizes, weights, flight speeds, and flapping frequencies can be expected of MAVs. Using these correlations, the effect of different parameters such as wing area, flight speed, wing aspect ratio, and body mass on aerodynamic performance can be predicted. This allows the researcher to compare flying objects that differ in size and weight by several orders of magnitude. Fortunately, there exists an abundant body of work with regressions drawn from data painstakingly collected in the field. Shyy et al. [42] has an excellent and concise review of all these correlations, so we will not repeat them in depth but instead briefly mention the major contributors. The bulk of this section then deals with the implications these correlations on MAV wing loading, size, weight, and ultimately derives from these factors the flow regime in which MAVs should be placed.

One of the earliest and most comprehensive investigators, Greenewalt [2,3] gives many correlations relating

wing span, wing area, and mass among birds of different species. He loosely and somewhat arbitrarily places all birds into three classes or models and extracts relations for wing loading as a function of wing area. In the same vein, Norberg [4] gives similar correlations for wing span versus mass and flapping frequency versus mass. Pennycuik [5] added to the database by fitting data for over 50 different species of birds and bats to develop predictions of flapping frequency as a function of body mass and wing area. Tennekes [43] ties all this together into his “Great Flight Diagram” which graphs weight and wing loading against cruising speed for all fliers from common houseflies to Boeing 747 passenger jets. Remarkably, even though there is some scatter from the mean, all fliers seem to roughly fall on the regression line given by simple dimensional analysis, as seen in Fig. 1.

2.1. Wing loading

The most important parameter governing the flight mechanics of a flying object is the “wing loading”, which is defined as the ratio between the weight of the object and the wing area. The standard values usually chosen for these two numbers are the maximum gross weight and the projected area of the wings on a horizontal plane. We start with the definition of the lift coefficient, C_L , as

$$C_L = \frac{L}{\frac{1}{2}\rho U^2 S}, \quad (1)$$

where L is the lift force, ρ is the local air density, U is the forward flight velocity, and S is the wing planform area.

In level flight the lift force equals the body weight, W , and so the wing loading can be expressed as

$$L = W = \frac{1}{2}\rho U^2 S C_L \Rightarrow W/S = \frac{1}{2}\rho U^2 C_L. \quad (2)$$

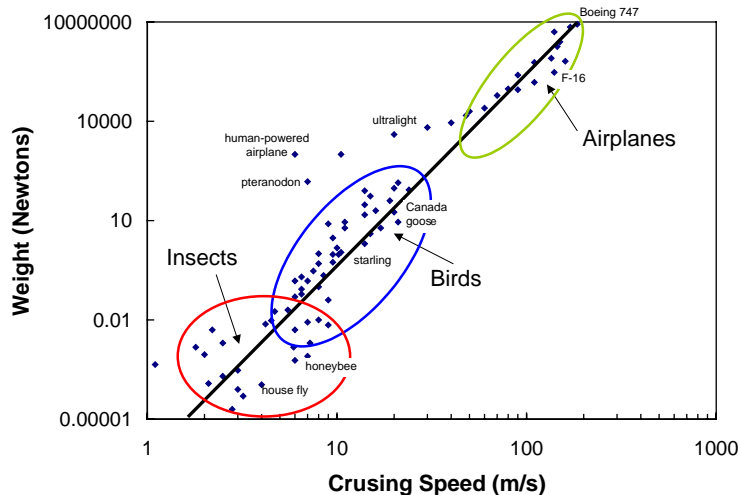


Fig. 1. Great diagram of flight. Adopted from Tennekes [43].

The wing loading is of importance when studying the flight mechanics of an object because it summarizes the opposing action between two classes of forces in flight: one is the gravitational and inertial forces, and the other is the aerodynamic forces that are responsible for creating lift and thrust.

From dimensional analysis, the first class of forces is proportional to the third power of the size ($\sim l^3$) of a flying object, while the second is proportional to the second power of the size ($\sim l^2$). Assuming geometric similarity, the wing loading can be rewritten as

$$W/S \sim l \rightarrow W/S \sim W^{1/3}. \quad (3)$$

As a result the wing loading is proportional to the first power of the size or to the $\frac{1}{3}$ power of the weight. Although a rudimentary analysis, it is found that both man-made (Fig. 2) and natural (Fig. 3) flying objects in

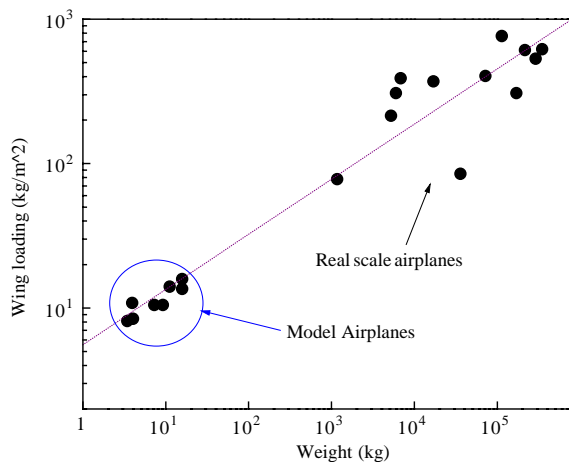


Fig. 2. Wing loading of man-made flyers versus weight ranging from 0.5 to 500,000 kg. Adopted from McCormick [44].

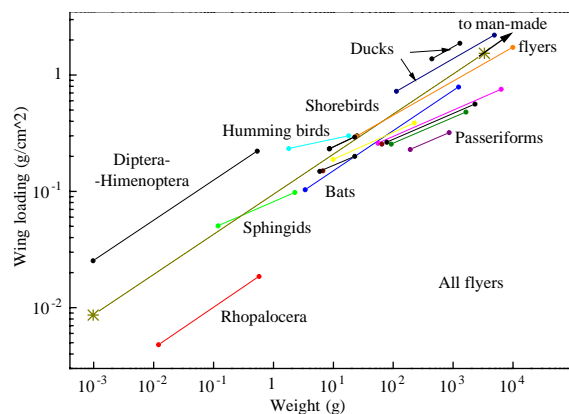


Fig. 3. Wing loading of insects and birds versus weight ranging from 1 mg to 1 kg. Adopted from Greenewalt [3].

general follow this rule, although some deviation is seen. Fig. 2 plots airplanes in size from model aircraft to full-scale propeller and jet aircraft. The straight line interpolating the data points taken from both full scale and model airplanes has a slope of approximately 0.33. The scatter for large aircraft can be largely attributed to performance aircraft designed for high maneuverability such as fighter planes or acrobatic stunt aircraft.

In Fig. 3, the weight ranges from 1 mg for small insects to 1 kg for heavier birds. Even though the data is more scattered, the slope of the interpolating straight line remains about 0.33. As a matter of fact, if the fitting line that passes through the two star symbols is prolonged toward the right (heavier flyers), it would overlap with the interpolating line of Fig. 2. Moreover, even though insects taken as a whole show an appreciable deviation with respect to the fitting line, each single species alone shows a behavior very consistent with the general trend. For example, the lines representing the species of *Diptera* and *Rhopalocera* are almost an order-of-magnitude off (in terms of wing loading) from the fitting line, but their slopes are again roughly 0.33. The conclusion from these observations is that there exists a “universal” law relating the wing loading to the size or weight of a flying object. In other words, *there is a maximum weight that can be carried by a flyer of a certain size; or vice versa, a minimum size given a certain gross weight.*

There are physical reasons that justify such a universal law although deviation does exist from it. The presence of the deviation is governed by aerodynamic and structural reasons. The upper boundary represents the fact that, given a certain size, lift force cannot be arbitrarily increased to balance a larger weight. For the upper bound, the two limiting factors are that of a maximum lift coefficient and of a maximum flying velocity that cannot be indefinitely increased for practical purposes. The lower boundary represents the fact that, given a certain size, the gross weight cannot be arbitrarily decreased. The limiting factor in this case is the strength of the materials used in the structure of the flyer, which cannot be arbitrarily increased in order to reduce the empty weight of the flying object.

Shyy et al. [42] notes that natural fliers face the same limitations in terms of power availability and structural limits. Birds use their pectoral muscles for downstroke motion and the supracoracoid muscles for the upstroke. Together, these muscles constitute up to 17% of the total weight and are estimated to provide up to 150 W/kg of power output. This represents the upper limit on power availability for natural fliers and Pennycuik [45] estimates an upper body mass limit of 12–15 kg. Structurally, high flapping frequency is not an option for larger birds since their bones cannot withstand the stresses imposed by moving such a large inertial load. Smaller birds and bats can flap at higher

frequencies due to reduced inertial loading, but they are still limited by the breaking stress of their hollow bones.

Once it is understood that the range of wing loading is limited by physical constraints, it is important to explain what role the wing loading plays in deciding a wing's efficiency and performance. A higher wing loading allows the flier to carry a larger payload, thus increasing the economy of the mission, or a higher capacity of fuel, thus increasing the range. In turn, a higher wing loading corresponds to a poorer performance. If a fixed wing device is considered, the take-off distance, the landing distance, and the turn radius increase with the wing loading, while the range decreases with it. This means lower agility and maneuverability together with shorter autonomy. The above consideration can be adapted and extended to flapping wing flyers as well. Furthermore, the power input per unit weight is proportional to the square root of the wing loading. Therefore, the more loaded the vehicle the less efficient it is, since more power is needed to carry the same unit load. Such considerations are of fundamental relevance in the design of an air vehicle once a performance envelope is specified.

While the scaling laws provide guidance on the weight expected for a certain wing loading, it should be emphasized that they are only a general guideline. Indeed, Fig. 3 shows that there is quite a bit of latitude and scatter, especially at the lower weight limits. This is good news for MAV designers and engineers, as it indicates they have room to improve their vehicles and technology before running into any physical limitation.

2.2. MAV size and weight

From Fig. 3 it can be seen that many different species of animals (particularly bats and hummingbirds) in nature fall within the size range of MAVs. Fig. 4 then

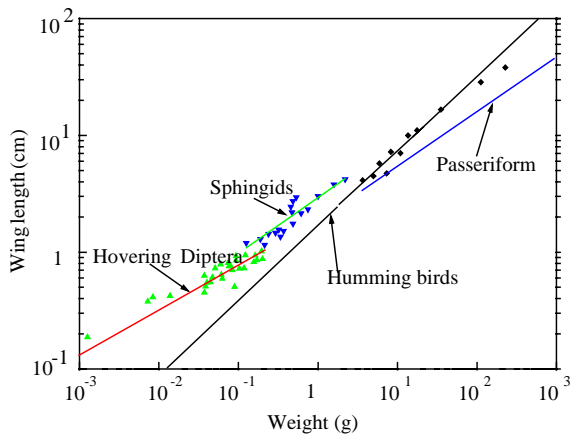


Fig. 4. Wing length and weight relation of flying subjects. Adopted from Greenewalt [3].

provides useful information on the relation between wing length and weight of insects and birds.

It is worth specifying that wing length is measured according to the biological definition and includes the wing from the tip to the first articulated joint. The wingspan is the largest dimension of a bird and is equal to twice the wing length plus the width of the body. In order to fall within the 15 cm maximum size requirement for MAV, the wing length of a comparably sized bird or bat is at most 7 cm.

Fig. 4 provides the following observations:

(1) Only some large insects, bats, and hummingbirds are within this size requirement.

(2) The weight ranges from 0.1 to a few grams for insects with wing length from 1 to 7 cm, or from 2 to 7 g for humming birds with wing length from 3.5 to 7 cm.

At this point it is also interesting to note that 15 cm is approximately the border between flyers capable of two different types of flight: flyers under this size are able to hover but cannot soar, while bigger flyers cannot hover (in the sense that they cannot keep a steady position with zero velocity with respect to the surrounding air) but they can soar. Following this observation, it seems that an ornithopter design is best for mechanical flyers below 15 cm in wingspan. Furthermore, a wingspan of 15 cm corresponds to a weight of 7–10 g.

2.3. Size and steady versus unsteady flow regimes

From Pennycuik [46] the relation between flight speed and the mass of a bird can be given by

$$U = 4.77m^{1/6}, \quad (4)$$

where U is the flight speed in m/s and m is the mass in grams.

Greenewalt [2] computed from statistical data the correlation between wing flapping frequency f (Hz), vs. wing length l (cm), to be

$$fl^{1.15} = 3.54, \quad (5)$$

while Azuma [47] showed that the correlations for wing flapping frequency (Hz) vs. mass, m (g), for large birds and small insects are

$$f(\text{large birds}) = 116.3m^{-1/6}, \quad (6)$$

$$f(\text{small insects}) = 28.7m^{-1/3}. \quad (7)$$

From Eqs. (4)–(7), relationships between wingtip speed and mass can be derived. These relations are

$$\text{Wingtip Speed (large birds)} = 11.7m^{-0.065}, \quad (8)$$

$$\text{Wingtip Speed (small insects)} = 9.7m^{-0.043} \quad (9)$$

and a plot of wingtip speed and flight speed versus mass of insects and birds can be generated as shown in Fig. 5. The flight of flyers can be separated into two

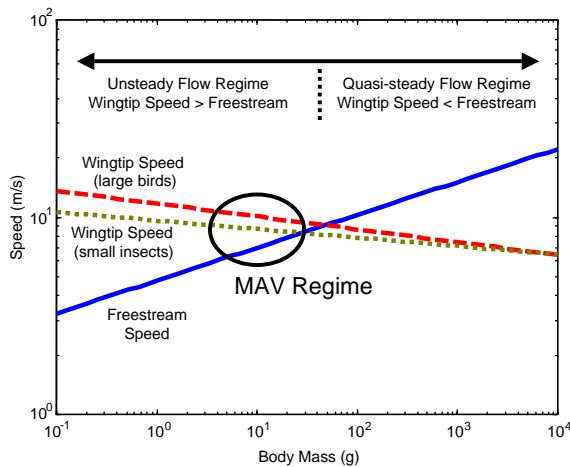


Fig. 5. Plot of wingtip speed and flight speed versus mass.

regimes: quasi-steady and unsteady. For larger flyers, their flights can be approximated by quasi-steady-state assumptions because their wings flap at low frequency (or hardly at all) during cruising. Hence the wingtip speed is low compared to the flight speed. So larger birds, such as eagles and seagulls, tend to have soaring flight and their wings behave like fixed wings. On the other hand, smaller birds and insects fly in an unsteady-state regime in which the wingtip speed is faster than the flight speed, e.g., flies and mosquitoes flap their wings at several hundred hertz. From Fig. 5 we conclude that MAVs operate in an unsteady-state flow regime in which the fluid motion is not constant over time and cannot be approximated by quasi-steady-state assumptions.

3. Vortex dominated unsteady aerodynamics

No exact analytic analysis of flapping flight yet exists, and given the considerable complexity of flapping flight, it is unlikely that one will emerge in the near future. As Shyy et al. [42] notes, birds attain their amazing flight performance by using adaptive feedback control of a variable geometry, flexible surface wing to manipulate and optimize various unsteady and three-dimensional flow mechanisms. A complete model of the system requires not only a prediction of the unsteady aerodynamics, but also a description of the time and geometry dependent aeroelastic interactions between the wing and the flow field. Nevertheless, it is instructive to examine simplified models that capture some aspect of the dynamics. As long as their underlying assumptions are kept in mind, these models can prove useful in design and testing of MAVs or in interpreting natural flier data.

Early work in bird flight attempted to extend quasi-steady linear aerodynamic theory to the realm of

flapping flight. For example, Greenewalt [3] assumed an elliptical lift distribution with “suitable correction factors” to model bird flight and then proceeded to estimate power and drag coefficients for various bird species. Pennycuik [45,48] theorized that a steady actuator disc producing constant momentum flux could represent the flapping wing and its aerodynamic force generation. Other researchers [49,50] adopted a quasi-steady vortex wake model to compute the induced velocities in a classical lifting line model of the wing. Ellington [51] however, in his 1984 seminal work showed that these quasi-steady analyses do not correctly predict the force magnitudes, particularly the lift coefficient, measured experimentally and other investigators [52] have also come to much the same conclusion. The major limitation of steady or quasi-steady analysis is that the motion of the wing causes an inherently unsteady wake with large vortices generated on the wing. If the flapping frequency is low compared to the flight speed, then the flow unsteadiness might be sufficiently muted for the quasi-steady assumption to remain valid, as in the case for gliding or soaring flight. However, high flapping frequency or very slow flight would certainly invalidate the quasi-steady assumption as the flow field is then inherently unsteady in nature.

One measure of the degree of unsteadiness is the reduced frequency, given by

$$k = \frac{\omega c}{2|V|}, \quad (10)$$

where ω is the wing angular velocity, c is the root chord length, and V is the forward velocity. The reduced frequency simply compares the angular velocity to the flow speed. As k rises, so does the flow unsteadiness. A fixed wing corresponds to $k = 0$. Note that the reduced frequency really is a metric specific to forward flight, since when $V = 0$, i.e., during hover, k goes to infinity or is undefined, depending on the angular velocity.

This article prefers to use the advance ratio to estimate flow unsteadiness. The expression is

$$J = \frac{U}{2\Phi b}, \quad (11)$$

where U , Φ , b , and f are the forward flight speed, total flapping angle, wing span, and flapping frequency, respectively. At first glance, the advance ratio appears to be just the inverse of the reduced frequency. However, by taking incorporating the wing span, it more accurately accounts for the three-dimensional nature of the flow since longer wing spans correspond to higher wing tip velocities and generally more unsteadiness. The breakpoint between quasi-steady and unsteady flow is when $J = 1$. For $J > 1$ the flow can be considered quasi-steady while $J < 1$ corresponds to unsteady flow regimes. Most insects operate in this unsteady regime. For example, the bumblebee, black fly, and fruit fly have

an advance ratio in free flight of 0.66, 0.50, and 0.33, respectively.

Hovering flight seems to be an exception to these general definitions. Furthermore, while hummingbirds and insects exhibit quite high wing flapping frequencies while hovering, steady-state models seem to adequately describe the aerodynamic forces involved. This is very surprising considering that dynamic stall, wing flexibility, and nonsteady wing motion are all basic characteristics of hovering. The only force needed, however, is lift to counterbalance the body weight, so perhaps a one-dimensional actuator disc model is appropriate since there is no linkage between lift and thrust generation. For those interested, Shyy et al. [42] again gives an excellent summary of hovering flight and the distinction between symmetric (wings are fully extended during the entire flapping cycle) and asymmetric (wings are flexed during the upstroke) hovering.

This section attempts to cover basic aerodynamic models in which unsteady flow mechanisms (primarily the generation of vortices) dominate. As noted previously, these models are appropriate in low advance ratio (i.e. high reduced frequency) situations, which occur whenever natural fliers are not gliding or soaring.

3.1. The clap and fling mechanism

Studying the wing motion of *Encarsia Formosa*, Weis-Fogh [53] found an unsteady inviscid high lift mechanism occurring at very low Reynolds numbers. Terming it the “clap and fling”, it advantageously made use of the interaction between two wings as they neared each other at the extreme ends of the stroke, providing that the total flapping angle was nearly 180° . Experimental observations led to a $C_L \cong 2.3$ for the wing, an impossibly high C_L for steady airfoils based on the wing’s critical Reynolds number, $Re_C = 20$. Fig. 6 depicts the wing kinematics and the consequent vortex development. The wing surfaces press together at the end of the upstroke for an extended period of time, mimicking a motion much like two hands coming together for a “clap”. As the wings separate and open for the next downstroke, they rotate around their trailing edges. The trailing edges remain adjacent and connected together until the included angle reaches approximately 120° . At this instant, the wings form a V-shape before they begin parting away from each other. The sudden translation of opposing section causes air to



Fig. 6. Weis-Fogh clap and fling mechanism illustrated on an *Encarsia Formosa*. From Ellington [54].

rush into the widening gap and produce high strength vortices of equal and opposite sign. This leads to large circulation and lift on the wing without the negatives of vortex shedding since the total circulation around both wings remains zero. The “clap and fling” also avoids altogether the Wagner effect (a time lag between the attainment of the instantaneous circulation value and the quasi-steady value around a wing due to the induced velocity field of shed vorticity).

Maxworthy [55] accounted for viscous effects, particularly the creation of a large leading-edge separation vortex, and showed that the separated vortices could significantly enhance circulation, which continued to increase even beyond included angles of 120° . Further, it was not necessary for the wings to come into complete contact to achieve high lift. Maxworthy also used a three-dimensional aerodynamic model to explain how, as the wings flung apart, a balance between pressure gradients and centrifugal forces creates a strong spanwise flow. This spanwise flow prevents the buildup of vorticity separating from the leading edge on the wing and safely deposits it into a tip vortex. In the two-dimensional case, this vorticity would be shed suddenly at the trailing edge, as in the Karman vortex street, resulting in a dramatic loss of lift. Ellington [11] commented that “near or partial clap and fling” was actually common in nature and could explain the flapping behavior of many birds and bats during take-off and landing, when extra lift generation is needed. Indeed, “clap and peel” is widely used, whereby two flexible wings (instead of rigid wings as assumed by Weis-Fogh) come into proximity and only meet at the trailing edge. As the leading edge rotates during the next flapping cycle, the wings peel apart at the trailing edges and unsteady vortices are again generated. Using the clap and fling mechanism, birds and insects take advantage of the high lift offered by unsteady aerodynamics achieved through simple kinematic wing motion.

3.2. Theory of the wake

Rayner [9,10] proposed a model whereby the forces on the wing could be calculated from the nature of the unsteady wake trailing the wings as they flapped. He assumed that rigid wings generated lift only during the downstroke and there is no loading on the upstroke and hence no trailing vortices. This results in a series of discrete elliptical vortex rings forming the wake, with one vortex ring created during each downstroke, as depicted in Fig. 7.

Experimental verification indicates that the vortex ring wake occurs only during mostly gliding or soaring flight, where the wings are flapped sparingly. For more active flight, the wings flap constantly and the resulting

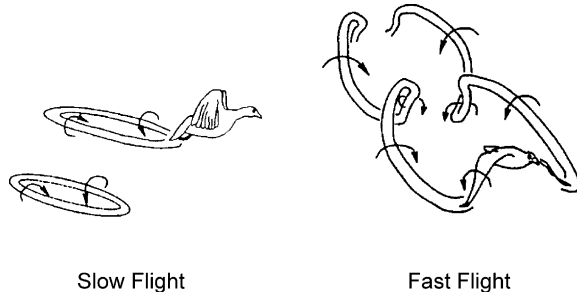


Fig. 7. Wake evolution for slow and fast flight. Adopted from Pennycuik [22].

wake is continuously shed in an undulating pattern from the wingtip.

From the Kutta–Joukowski theorem, the lift of a 2D section of the wing with a freestream density of ρ_∞ , a freestream speed of U_∞ , and a circulation distribution around the wing of $\Gamma(y)$ is

$$L(y) = \rho_\infty U_\infty \Gamma(y). \quad (12)$$

And hence the total lift is given by

$$L = \int_{-b/2}^{b/2} \rho_\infty U_\infty \Gamma(y) dy. \quad (13)$$

The total drag corresponds to

$$D_v = - \int_{-b/2}^{b/2} \rho_\infty w(y) \Gamma(y) dy \quad (14)$$

where w is the velocity induced by the vortex.

Imposing the Kutta condition, which requires that the flow meets smoothly at the trailing edge without any velocity discontinuities, uniquely determines the value of circulation $\Gamma(y)$ for the airfoil and therefore the lift on the airfoil. In order to relate $\Gamma(y)$, the airfoil circulation, to the circulation $\Gamma_w(y)$ in the wake, we make use of Kelvin's circulation theorem. For a homogeneous, incompressible inviscid fluid the circulation remains constant in time, i.e.,

$$\frac{D\Gamma}{Dt} = 0. \quad (15)$$

Accordingly, if the wing starts from rest then the total circulation is zero and must remain so for all times thereafter. Therefore, any $\Gamma(y)$ generated on the wing must be matched by a $\Gamma_w(y)$ in the wake, which has an equal but opposite strength, so that $\Gamma(y) = -\Gamma_w(y)$. By using this relation and Eqs. (13) and (14), the lift and drag on the wing can be computed from the circulation in the wake.

For vortex rings, the size of each ring in the spanwise and streamwise dimensions is calculated from key flapping parameters and wing length, while the ring circulation is conditioned on the balance between the generation of wake momentum equaling the total vector force of weight and drag.

The model allows for stroke averaged estimates of lift and thrust as well as the power requirements. It also accounts for some wing parameters such as wing length, flapping angle, and flapping frequency. However, the details of wing kinematics themselves are largely ignored and the modeling of the wake does not allow for a time history of force production during the flapping cycle. Ignoring wing geometry and profile, wing kinematics, and the vortex shedding in the wake greatly simplifies the aerodynamic analysis to just the unsteady history of the wake. This is both the blessing and the curse of the model. It remains extremely challenging to get an accurate measure of the wake evolution, due to wake diffusion and convection and the rapid rollup of the wake behind the bird. Still, Vest and Katz [55] showed in their study that the momentum in the vortex rings was only 65% of the momentum needed to balance the weight of the bird.

3.3. Rotational lift and wake capture

Dickinson [13,52,56] has extensively studied the effect of wing rotation during the transition from downstroke to upstroke in a mechanical model of the *Drosophila melanogaster* wing. Fig. 8 depicts the basic mechanism. There are three distinct phases. First, during the downstroke the wing translates at a constant velocity U at a given angle α_d . Rotation of the wing around an axis running through the chord plane then occurs at a constant angular speed. Finally, the wing translates at speed U during the upstroke with a predetermined angle α_u . This idea follows from observations of small insects and hummingbirds, which utilize this wing flip motion in their hovering flight modes and it allows the wing to

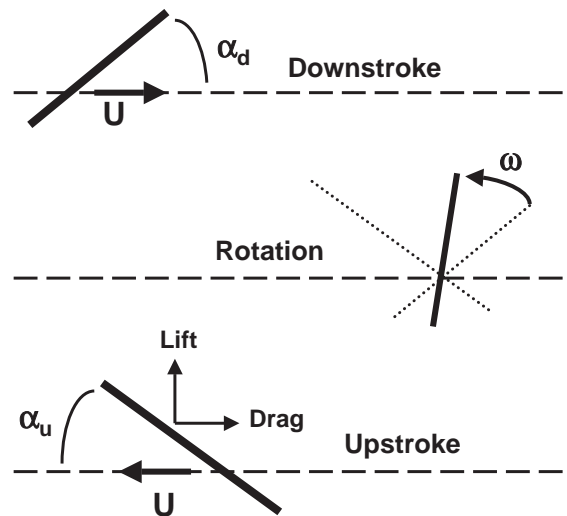


Fig. 8. Schematic of wing rotation. Adopted from Dickinson et al. [13].

maintain a positive angle of attack (AOA) through both the downstroke and upstroke.

In their first study, Dickinson [57] discovered that at the onset of rotation, two vortices are created. One is a bound vortex attached to the wing surface facing the direction of rotation. The second vortex, termed the “mirror vortex”, is a free vortex of equal and opposite strength to the bound vortex. This free vortex sheds from the surface opposite the direction of rotation. When the rotational motion ends, the bound vortex splits into two vortices that shed from the leading and trailing edges. Dickinson discovered that if the rotation occurs near the trailing edge of the wing, the mirror vortex becomes captured by the wing and adds to lift generation. If the rotation axis resides near the center chord point, the wing captures two vortices of equal and opposite strength, hence negating their lift contribution. Choosing the rotation axis close to the leading edge leads to the capture of the mirror vortex underneath the wing and results in negative lift generation. Fig. 9 depicts the three situations.

Wing rotation created lift even at zero AOA and appeared to enhance it for all other angles of attack tested. The drag coefficient also improved and was even slightly negative at zero AOA.

The mechanism of wake capture also proved significant in these experiments. If a wing translates through a series of vortices (such as a von Karman street) created by the previous stroke, then it would encounter a high velocity fluid stream that could speed the fluid velocity in the direction of translation and add to lift production. Dickinson found that if the wings translated backwards through a wake created during the previous stroke, then the lift could be greatly increased for all angles of attack. He measured transient lift coefficients as large as 4 for high AOA wing motion.

In later studies Sane and Dickinson [52] investigated varying the wing kinematic parameters and their effect on lift and drag production. They noted that while quasi-steady analysis yielded time averaged lift coefficients which reasonably matched the time averaged experimental lift coefficients, the transient lift coefficients were not well matched. The situation with respect to drag is even worse, with quasi-steady drag coefficients off by a factor of 3 and peak drag coefficients mismatched by a factor of 6. Clearly rotational lift and wake capture are large unsteady mechanisms that can improve or degrade severely the aerodynamic force generation for flapping wings.

3.4. The unsteady leading edge vortex

Most studies of insect and bird flight have assumed either quasi-steady aerodynamics or some inviscid formulation, such as the doublet-lattice method for numerical simulation. However, work by Dickinson and Gotz [31], a CFD study employing a fully viscous code by Liu et al. [41] and experimental research by van den Berg and Ellington [34,54], indicates that an unsteady vortex bubble caused by flow separation from the sharp leading edge can explain the high lift characteristics flapping flight. For instance, insect wings in steady flow typically exhibit a $0.6 < C_L < 0.9$, yet the mean C_L required for trim flight far exceeds this requirement, sometimes by a factor of 2 or 3 [54]. Accordingly then, there must be some unsteady high lift phenomena that make up for the deficiency in lift calculated from steady-state aerodynamics. The unsteady leading edge vortex has long been the prime candidate, but two-dimensional studies showed that lift enhancement was only limited to 3 or 4 chord lengths of travel before vortex breakdown occurs [31].

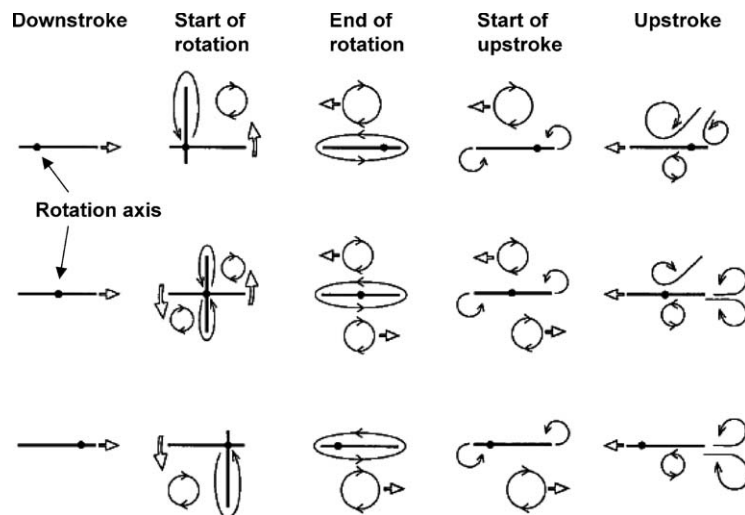


Fig. 9. Vortex development during rotation. Adopted from Dickinson et al. [57].

However, as seen in Figs. 10 and 11, the unsteady vortex does not breakdown. The reason is that the flow is *fully three-dimensional*; a strong spanwise flow exists that stabilizes the vortex. This spanwise flow convects the vorticity out toward the wing tip, where it joins with the tip vortex and prevents the leading edge vortex from growing so large that breakdown occurs. In fact, Maxwell first discussed these phenomena in his analysis of the clap and fling mechanism!

CFD work by Liu and Kawachi [58] examined the underlying physical processes in the growth of this

unsteady leading edge vortex on both flapping and rotary wings. They found that during the first half of the downstroke, an intense spiral-shaped leading edge vortex with strong axial flow forms and causes a low pressure region to grow on the upper wing surface. During the latter half of the downstroke, another leading edge vortex forms, but it runs from the tip toward the base of the wing due to the low pressure area near the base from the first vortex. During supination (the transition from the downstroke to the upstroke) these two vortices merge into a single hook-shaped



Fig. 10. Smoke visualization of the strong spanwise flow of the unsteady leading edge vortex (seen in blue). From Liu et al. [41].

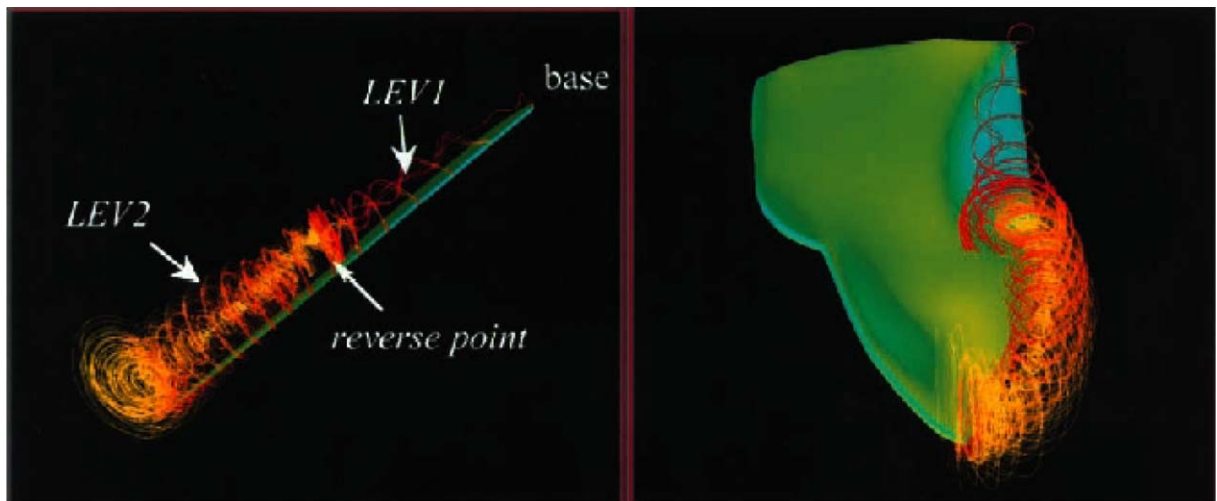


Fig. 11. CFD simulation of the unsteady leading edge vortex. From Liu et al. [41].

vortex that quickly becomes deformed and then sheds from the trailing edge. At the start of the upstroke, the flow is quite smooth over the entire wing on both the upper and lower surfaces. During the latter half of the upstroke, another leading edge vortex grows on the underside of the wing and causes a large negative lift force. At pronation (the transition between the upstroke to downstroke), this vortex rolls over the leading edge and is shed, along with a small trailing edge vortex on the lower surface and a shear layer vortex on the upper surface. The growth and shedding of the leading edge vortex is subject to many forces: centrifugal, Coriolis, and dynamic pressure gradients arising from both the vortex's spanwise velocity gradient and the axial velocity gradient through the leading edge vortex itself. Finally, Liu and Kawachi [58] estimated that approximately 80% of the total lift force was generated during the downstroke, with the remainder produced on the upstroke.

3.4.1. Unsteady leading edge vortex lift and thrust production

Other studies [59–62] shed light onto the nature of the unsteady leading vortex and its effect on lift and thrust generation for MAVs. The focus was to understand how the unsteady leading edge vortex forms on a typical sized MAV wing (7 cm span), find which areas of the wing were responsible for lift and thrust generation, map the time history of the lift and thrust generation during a single flapping cycle, and determine the relationship of lift and thrust as a function of the advance ratio.

Smoke wire flow visualization by Ho et al. [59] is shown in Fig. 12 and it captures the formation of a leading edge separation bubble during the downstroke of a 7 cm span and 3 cm chord paper membrane wing.



Fig. 12. The unsteady leading edge vortex as seen from behind and below a MAV wing. From Ho et al. [59].

At the start of the downstroke, the flow stagnates at the leading edge of the wing. The stagnation line progressively moves to the upper surface of the wing, thereby forming a leading edge vortex. This vortex grows and attains its maximum size near the middle of the downstroke and it finally sheds at the start of the upstroke. This leading edge vortex is accompanied by a strong outward spanwise flow. The spanwise flow helps stabilize the vortex in the mid-span section of the wing through vortex stretching. The spanwise flow decelerates towards the tips and the vortex core increases in size.

The size of the unsteady leading edge vortex was observed to depend on the advance ratio. For large advance ratios ($J > 1$, quasi-steady flow), no vortex was seen and the flow was always attached. However, as the advance ratio decreased below unity, the unsteady leading edge vortex appeared regardless of the chord size of the wing. For $0.25 < J < 0.5$, the diameter of the unsteady leading edge vortex was 3–4 cm near the mid-span region.

The low pressure region created by the streamline curvature associated with the vortex accounts for the lift produced on the wings. Fig. 13 graphs the correlation of vortex formation with unsteady lift measurements. The lift force reaches a maximum value near the mid-downstroke region, which is about the time where the separation vortex attains its maximum size. As the vortex sheds, the lift force decreases and is negative during the upstroke. Previous studies corroborate these results and further point to the lift force being primarily produced during the downstroke with its maximum being located near mid-downstroke [7,58,63]. The negative lift portion is attributed to a vortex that grows underneath the wing during the upstroke that is smaller than the separation vortex formed on the upper surface.

The separation vortex appears at advance ratios below order one and accounts for the unsteady lift force. Accordingly, the vortex strength depends on the

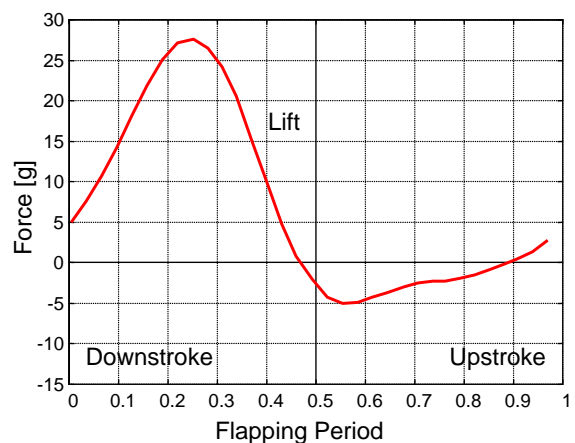


Fig. 13. Phase average lift during one flapping cycle.

wing speed, which is directly proportional to the flapping frequency. Greater vorticity on the upper surface translates to lower pressure and leads to a greater lift force. Fig. 14 shows the typical behavior of the lift coefficient as a function of advance ratio for flexible flapping wings. At large advance ratios, the lift coefficient is at a minimum with a value below one as would be expected for such a low chord Reynolds number flow ($<10^4$). As the advance ratio drops, the lift coefficient starts rising with a consistent inverse power law. A lift coefficient of 3 is common for a $J = 0.33$. This inverse power law implies that the lift force is directly proportional to the flapping frequency as was expected from the vorticity's dependence on flapping frequency. Overall, for vortex lift augmentation to be significant, the wings must operate in a fully unsteady flow regime, i.e., they must flap at higher flapping frequencies to generate wingtip speeds comparable to or greater than the freestream velocity.

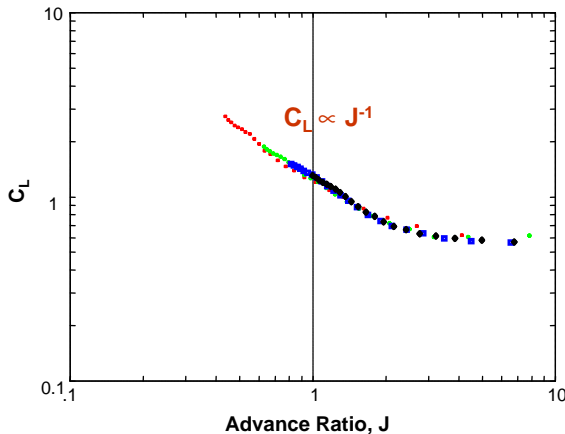


Fig. 14. Lift coefficient dependence on advance ratio.

To further test the claim that lift is produced by the separation vortex, two wings were compared where the inboard region of one wing was arbitrarily removed (see Fig. 15). Since the wing speed varies along the span, the strength of the separation vortex and thus the lift will also vary in the same manner. The linear speed of the wings is higher towards the tips and leads to stronger amounts of vorticity in the outboard region of the wings. Therefore, it can be expected that the bulk of the lift is produced in the wings' outboard region. In Fig. 15, both wings produced the same lift coefficients, and removal of the inboard region did not have an effect since the vorticity outboard was not affected. However, notice that the thrust performance was significantly altered. As will be discussed later, this change in thrust performance is attributed to the change in vortex shedding from the wing. Since the trailing edge differs greatly between the two wings, it is not surprising that the shedding from these two wings proceeded differently and led to the disparity in the thrust performance.

While the lift coefficient was consistently observed to be inversely proportional to the advance ratio, the thrust coefficient did not have a consistent power law. Fig. 16 graphs one example of thrust behavior as a function of advance ratio. Furthermore, the power law shown is higher than would be expected if the thrust coefficient were to also depend on the vortex strength. It is believed that the thrust production is intimately tied with the vortex shedding and the trailing edge deformation. Notice that for thrust production to increase, the wings must operate in a fully unsteady regime.

Fig. 17 shows an example of the unsteady thrust measurements. Notice that thrust is not produced until the later part of the downstroke and well into the upstroke, a time where the separation vortex is being shed according to the flow visualization. A wing can produce a separation vortex of some strength and

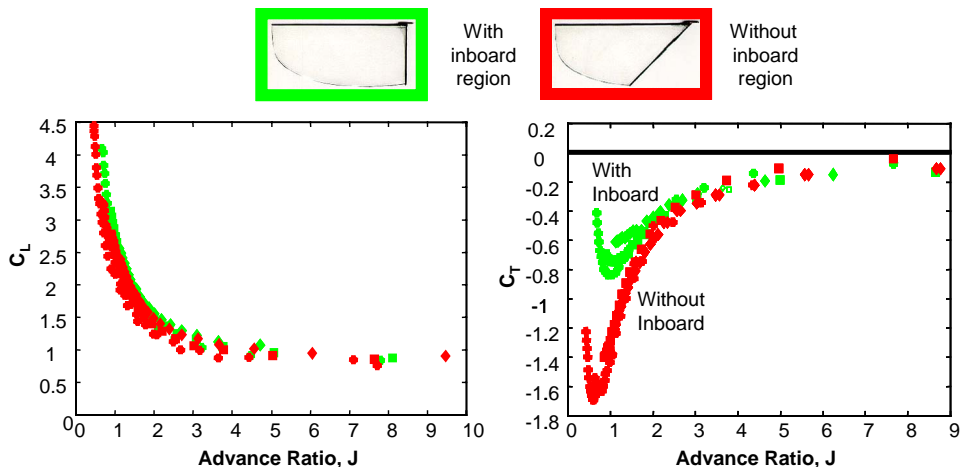


Fig. 15. Lift and thrust production as a function of wing area.

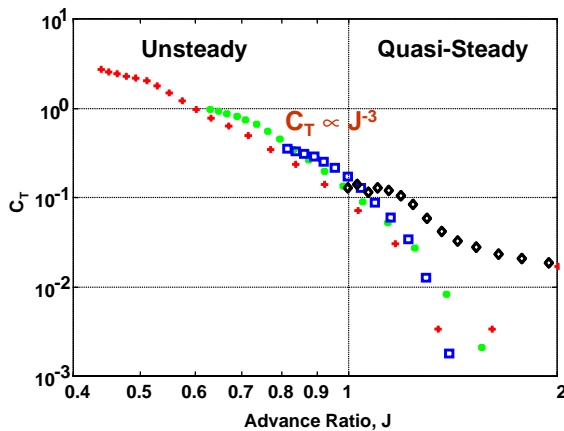


Fig. 16. Thrust as a function of advance ratio.

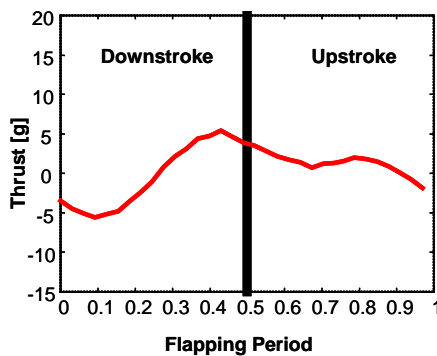


Fig. 17. Thrust phase average.

thereby a fixed amount of lift; however, depending on the wing's flexibility and orientation, that vorticity could be shed differently.

4. Aeroelastic coupling and its importance

Although many researchers have noted the importance that flexible wings play in the aerodynamics of flapping flight, there exist precious few studies dealing with flexible rather than rigid wings or airfoils in flapping flight. Numerical and experimental work so far has centered on rigid wings because the aeroelastic interaction between the wing and surrounding fluid could then be neglected and the overall complexity of the problem is greatly reduced. Given the already knotty fluid mechanics problem at hand, it is reasonable to simplify the problem in order to start the analysis. Computational means and the fluid mechanical analysis have advanced to the point, however, where the aeroelastic interaction can now be included.

Understanding the fluid–structure interaction is more fundamental than simply plugging a hole in the existing

analysis. The design of MAV wings for slow forward flight requires knowledge of how a highly flexible airfoil will deform under aerodynamic loading and the effect of that deformation on airfoil efficiency. The wing shape itself depends upon many physical parameters such as camber, chord and span length, and, most importantly, the mass and stiffness distribution. But dynamic quantities such as the time dependent pressure loading, wing speed, freestream velocity, and local acceleration of the wing surface also directly drive the instantaneous wing deformation. Therefore, it is the dynamic coupling between the wing and surrounding air that decides the final lift and thrust force.

With this in mind, it poses the interesting question: can manipulation of the wing's aeroelastic properties lead to improved performance? Clearly, changes in the wing deformation will affect the aerodynamics and so it seems quite possible that changes in the physical properties of the wing could yield better performance. In many respects, this is an inverse problem, where the desired result is known, but not the wing shape needed to achieve it. How this could be accomplished both with passive and active control methods remains an open research question, but one worth future exploration. The first step is to examine past investigations of airfoil aeroelastic response to unsteady flows.

4.1. Aeroelastic models

Smith [35,64,65] developed perhaps the first numerical simulation to account for aeroelastic coupling in flapping flight. He modeled the aerodynamics of a tethered flapping sphingid moth *Manduca Sexta* using an unsteady aerodynamic panel method and computed the effect of wing flexibility with a FEM. The aerodynamic solver was an unsteady three-dimensional inviscid flow solver while the finite element solver modeled the wing surface as a quadrilateral orthotropic stress membrane. The simulation showed a switching pattern in the direction of the aerodynamic force that decoupled the force direction and magnitude during the upstroke and downstroke. The forces were in opposite directions during the downstroke and upstroke, but the downstroke force magnitude was larger than the upstroke, indicating that the moth would travel in the direction of the force produced during the downstroke. The FEM discovered that the initial wing stiffness was too great, leading to overestimation of force magnitudes compared to experimental values. This confirmed the necessity to properly account for the wing flexibility when determining aerodynamic forces.

Shyy et al. [36] compared the lift to drag (L/D) performance of three airfoils of the same camber but with different membrane flexibilities in a sinusoidally oscillating freestream. In comparison to the rigid wing, a highly flexible latex membrane wing exhibited better

L/D performance at higher angles at attack but worse L/D ratios at lower freestream velocities due to the decreased pressure differential between the upper and lower membrane surface. A hybrid wing exhibited equal to or greater than L/D improvement at all angles of attack compared to the flexible wing and it was not as sensitive to L/D drop at lower freestream velocities. From this, they drew the conclusion that modulating the flexibility could improve the aeroelastic characteristics of the wing and ultimately the flight performance.

Shyy et al. [66] carried this concept further and developed a CFD model to test a rigid CLARK-Y wing against the same wing but with a massless flexible membrane on the upper surface. Again both wings were placed in a sinusoidally oscillating freestream. The flexible membrane wing again bested the rigid wing, with much less drop in C_L and less fluctuation in the power index $C_L^{3/2}/C_D$. This demonstrated the value of the adaptive airfoils in a fluctuating freestream.

4.2. Flexible and rigid wing lift and thrust production

Fig. 18 shows wind tunnel test results of rigid *cicada* wings and flexible titanium-alloy wings without the support of carbon fiber rods at the leading edges. The artificial wing was flexible in the spanwise direction along the leading edge. For this wing, the spars were etched from 300 μm thick titanium while 20 μm of Parylene-C were evaporation deposited on the spars to form the wing membrane. Both wings had a 7 cm span and 3 cm chord. The tests demonstrate that spanwise stiffness along the leading edge is an important factor in

lift production for flapping flight. For the same size of wings, cicada wings with rigid leading edges produced larger lift coefficients compared to wings having flexible leading edges, with the lift increase rising rapidly as the unsteadiness increases. In the regime of advance ratio less than one, i.e., unsteady flow, the lift coefficients of wings with rigid leading edges increased rapidly while that of flexible leading edges lost lift. This is likely due to the presence of large deformations along the leading edge of the flexible wing that disrupted the unsteady leading edge vortex, resulting in a loss of vortex lift. As the influence of the vortex rises with the degree of flow unsteadiness, this leads to a greater divergence in lift performance, as evidenced by the experimental results.

Stiffness distribution also plays a large role in thrust production because of the tightly coupled aeroelastic nature of the system. Any change in the manner of wing deformation will cause a change in the aerodynamic performance and vice versa. This coupling is especially strong when dealing with thrust generation since it depends on vortex interaction with the wing. Hence, modifying the stiffness distribution will change the wing deformation and the nature of the vortex interaction. For instance, two identical wings were tested and compared according to the C_T , defined as

$$C_T = \frac{T}{\frac{1}{2}\rho U^2 S} \quad (16)$$

where T is the thrust force, ρ is the local air density, U is the forward flight velocity, and S is the wing planform area. Both wings have the same sized carbon fiber spars, but one wing has a paper membrane while the other has

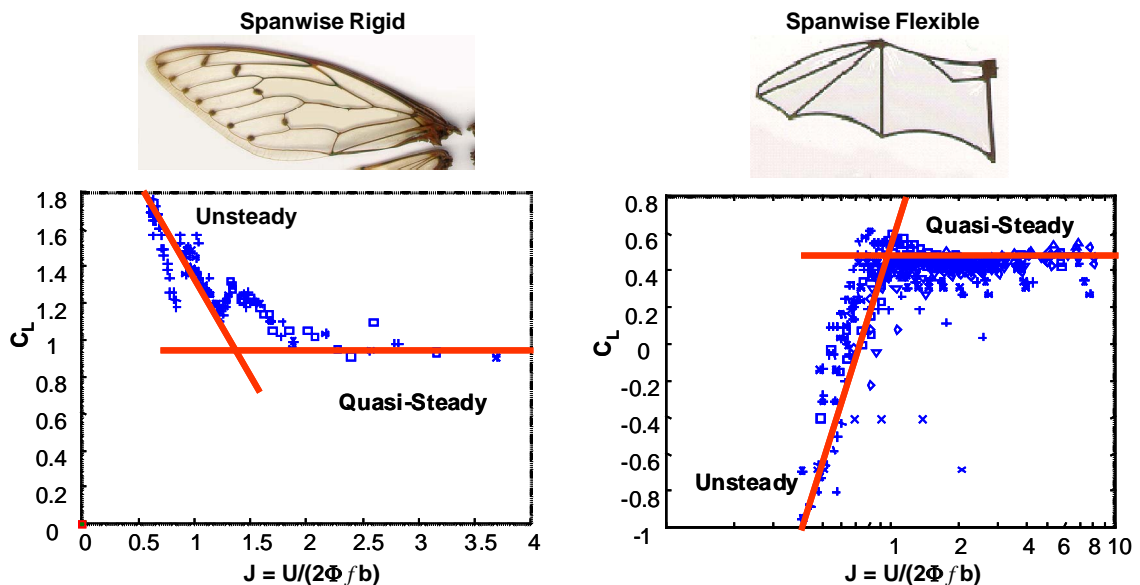


Fig. 18. Stiffness distribution effect on lift performance.

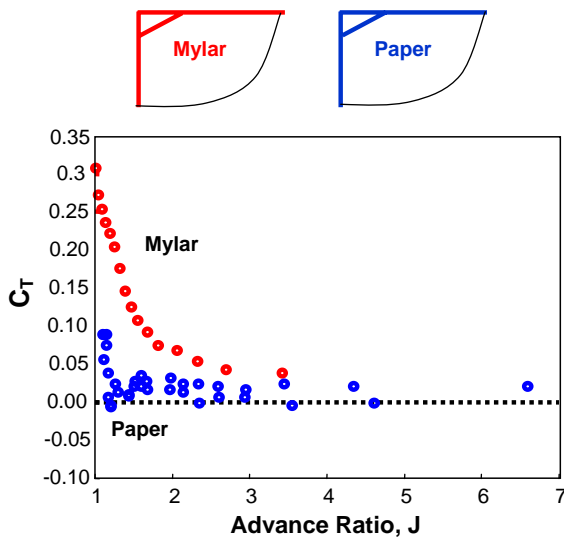


Fig. 19. Stiffness effect on thrust production.

a Mylar membrane. The paper membrane is less flexible than the Mylar wing due to the higher stiffness of paper. As seen in Fig. 19, the thrust performance differs greatly and it diverges faster as the advance ratio decreases. While this helps demonstrate the effect of wing stiffness, it does not provide a guide finding the proper wing membrane stiffness distribution for optimal force production.

It was observed from comparisons over a large number of different wing designs tested that stiffer membrane wings did not produce thrust, while more flexible wing membranes did. A stiff wing maintains a large frontal area throughout the flapping cycle when feathered normal to a highly inclined stroke plane, thereby leading to more drag. Keeping the results in Fig. 18 in mind, an attempt at introducing a known amount of flexibility in the wing design was made. The results in Fig. 18 accentuate the idea that the outboard region should be kept rigid to promote lift and flexibility should be permitted in the inboard region to allow for thrust. Fig. 20 shows how the membrane and wing are formed. Sweeping the leading edge of the membrane to some angle and attaching it to a square frame causes the membrane to bulge near the root chord. This shape, initially made of vellum paper, is rather flexible in the inboard region and greatly deforms during the upstroke, while the outboard region does not deform as much during the entire flapping cycle. Fig. 20 shows the positive thrust performance of the designed wing, which has the same planform area as that described in Fig. 18. According to flow visualization, a flexible wing affects the timing, strength, and shedding of the separation vortex as well as having a variable frontal area during the flapping cycle unlike the rigid wing.

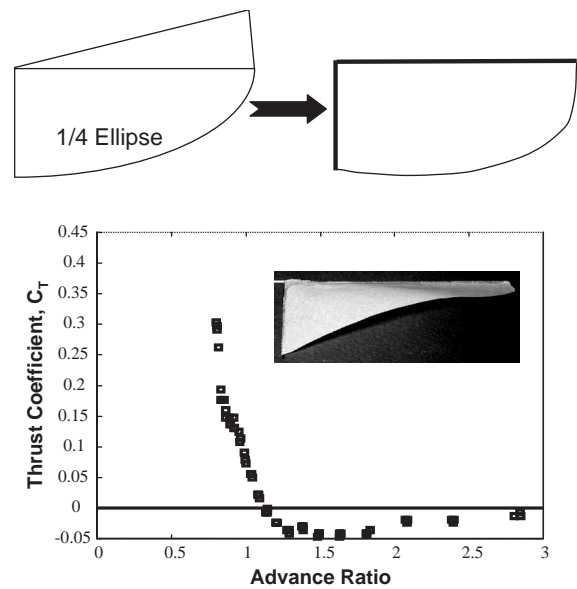


Fig. 20. Effect of preplanned flexibility on thrust.

The effect of flexibility was further highlighted when attempting to mass produce the wing design in Fig. 20. The wing spars were titanium with a carbon fiber spar re-enforcement. The membrane used Parylene, a flexible plastic material. Fig. 21 compares two generation of the titanium–parylene wing with the original paper wing described above. Since a thin parylene membrane cannot hold its shape, two diagonal spars were placed. The lifting ability of the first generation metal wings closely match that of the paper wings for large advance ratios. However, at some point, the metal wing performance falls short of the paper wings. Flow visualization of the metal wings indicated that the outboard region was too flexible, effectively feathering the outboard region towards the horizontal and disrupting the spiral leading edge vortex. For this reason, the second generation wing was designed to further re-enforce the outboard region by further sweeping back the diagonal spar. As Fig. 21 shows, the second generation metal wings now match the performance of the paper wings.

The general observations concerning the importance and effect of wing stiffness appears to hold true for all wings, whether they are natural or artificial. A number of different types of comparably sized insect wings (taken from a *chalcosoma* beetle, *callipogon* beetle, and a *cicada*) were tested at comparable parameter ranges to the previously described man-made wings. The wind tunnel tests showed that while the insect wings generated sufficient lift for flight, the wings produced considerable amounts of drag and did not meet the thrust requirements for level, forward flight. Clearly, these wings must be capable of thrust generation as the insects show no

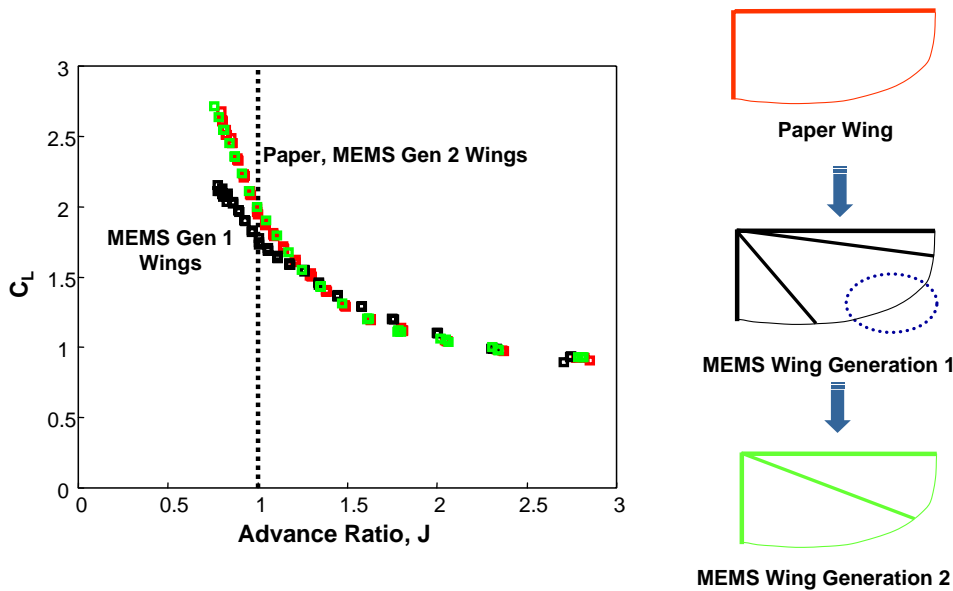


Fig. 21. Effect of overall stiffness distribution on wing development.

difficulty flying about in nature. The reason for the discrepancy between the wind tunnel tests and natural insect flight is that the wings were desiccated and hence had stiff wing membranes. When the insects are alive, the wing membranes were flexible and therefore generated thrust in much the same way as the flexible artificial wings. The testing of the man-made wings demonstrated that Nature had, through eons of evolution, already found the answer to wing membrane design for efficient operation in this unsteady flow regime.

5. Open loop control of separated flows

Given the flight environment envisioned for MAVs, one where the time varying forces and a large degree of flow separation exists, perhaps it can be instructive to review both how natural fliers achieve their outstanding flight performance as well as methods devised by man to expand the flight envelopes of fixed airfoils facing large-scale flow separation. This section highlights open loop flow control systems, although in the case of natural fliers the distinction between open and closed loop flow control often blurs. Animals and insects employ both active and passive measures to increase their aerodynamic performance and often it becomes difficult distinguishing one from the other. For man-made systems, this task is clear cut.

Regardless, an examination of open loop systems reveals the depth of research already conducted on vortex control for both steady and unsteady phenomena. Much of the aerodynamic work deals with delta

wings and prevention of vortex burst, which is an instability that destroys the coherence of the leading edge vortex and the extra vortex lift it provides. Analysis of the dynamic stall vortex (DSV) found commonly on rotorcraft and the prevention of flutter on fixed airfoils is also included in this section. Notice that all these processes also occur to some extent in flapping flight. The unsteady leading edge vortex relates directly to the steady leading edge vortex found on delta wings. The DSV is often mentioned as a mechanism in flapping flight, particular when discussing the clap and fling technique and the unsteady leading edge vortex. Flutter is simply an aeroelastic mechanism caused by the detrimental interaction between the airfoil structural vibrations and the aerodynamic loading. Flutter has not been observed for natural fliers, but the aeroelastic coupling seems inherent for flapping flight. So it appears that much can be learnt already from existing research on separated flow control and translate it that to the study of flapping flight.

This is not to say, however, that the specific means of flow control devised for fixed and rigid airfoils will work on flapping wings. Indeed, many of the methods require bulky and cumbersome internal piping and pumps to inject or extract momentum into or from the flow field. Other control techniques involve relatively heavy ceramic materials, which cannot be used on lightweight flapping wings due to inertial power constraints. Nevertheless, the idea of controlling the vortex flows on fixed airfoils can be appropriately modified to the case of flapping airfoils. An example comes in the last example of the section, where MEMS check-valves alter the pressure distribution near the leading edge of a flapping

MAV wing and can significantly improve the lift and thrust production.

5.1. Natural flier techniques

Bird and insect flight represents perhaps the best examples of open loop control of separated flow over a wide range of flight conditions. Over 300 million years of evolution has created several ingenious adaptations, from the complex 3-D corrugations seen on the wings of dragonflies that promote a laminar separation bubble for enhanced lift at low Reynolds numbers to the complicated wing root articulation motion and fine feather and wing tip control exhibited by birds which maximize lift and reduce drag during both the downstroke and upstroke of the flapping cycle.

Birds are known for their control of the angle of attack (AOA) using such means as passive elastic deformation of the wing feathers, and use of articulation muscles in the shoulder, elbow and wrist [67]. This allows for precise control of the vortex and wing interaction, which as noted previously, is particularly important for thrust production. Furthermore, the bird's body profile itself can enhance or promote separation and laminar-turbulent transitions, as well as trap separation bubbles for added lift [68]. The tail surface also serves many roles, from acting as an additional lifting surface, to drag reduction by preventing flow separation, and finally to improve control and stability [69]. There even exist passive eddy flaps that are self-activated to prevent flow separation for situations such as landing [70].

The wing shape itself is also well known to aid in the remarkable flight performance of birds. For example, previous work has shown that the shape of the trailing edge [71], wing camber and feather transmissivity [72], and the influence of the trailing edge notch [73] all demonstrate that evolutionary adaptation has produced extremely specialized aerodynamic enhancements for wing shapes.

Finally, changes in wing and tail kinematics can cause gross changes in aerodynamic performance. For instance, Brown [74] noted the flexure of the wrist during the upstroke that likely assists in maintaining thrust by reducing the frontal area and resultant drag. Many researchers have recorded complicated wing kinematics during the flapping cycle (see for example, Tobalske and Dial [16]) and remarked on the adaptation of the wing motion as a function of forward flight speed or maneuvering motion.

5.2. Delta wing vortex control

Once the flow field separates at the leading edge and vortex generation occurs, the physical situation becomes independent of Reynolds number. The methods of

vortex control in this case can also then be applied to a wide range of Reynolds number regimes. Since leading edge flow separation occurs for both delta wings and flapping fliers, it should be possible to take advantage of the knowledge gained from delta wing control and apply it to the flapping flier. If such control can be exercised over the airfoil, then dramatic reductions in the lift-to-drag polar are possible. For example, actuating in such a way that increases the vorticity without expanding the vortex size would lead to higher lift without additional drag. Control of vortices over delta wings has been a rich research topic and a wide variety of actuation schemes have been tested to control the separation, dynamic behavior, and breakdown of vortex flows. This section is not an exhaustive review, but it provides some illumination of the major research approaches to this problem.

The most distinguishing feature of the delta wing flow field is the existence of a pair of well-organized and highly energetic counter-rotating leading edge vortical structures. These vortices form at a moderate AOA as a result of flow separation along the leading edge. This leading edge vortex forms in both steady and unsteady flows. The high swirl velocities in leading-edge vortex flow induce a large suction force (the aptly named vortex lift phenomenon) on the delta wing surface, which enhances the overall aircraft performance. These leading edge vortices remain robust even at relatively high AOA when most conventional unswept wings experience static stall. Unfortunately, at high AOA the vortices develop a large-scale instability that is characterized by rapid deceleration and eventual stagnation of the axial velocity along the vortex core. This leads to a strong oscillation and total breakdown of the vortical structure. This phenomenon is commonly known as vortex breakdown or vortex burst and results in a dramatic loss of lift.

Both leading and trailing edge suction and blowing has been comprehensively studied, yet all the control methods proved to be limited to only certain operating parameters or required power intensive actuation systems. For example, Gu et al. [75] studied the effects of suction, blowing, and alternate suction-blowing applied in the tangential direction along a rounded leading edge to prevent vortex breakdown. McCormick and Gursul [76] and Badran et al. [77] applied suction along the upper surface of a sharp leading edge, and they found that suction properly placed near the separation point could displace the vortex breakdown location and prevent breakdown over the wing. Lee [78] verified that 1-mil stainless steel sheets on a rounded leading edge could shift the positions of leading edge vortices over the wing, leading to a considerable change in the pressure field around the aircraft and therefore the aerodynamic loading. By properly sizing the actuators near the separation point along the leading edge, they could interact efficiently with the unsteady flow instabilities to generate large aerodynamic force changes.

Huang et al. [79] extended this work and demonstrated that a “bubble” type MEMS actuator array on the rounded leading edge could produce the same change in aerodynamic forces. This proved that small actuators near the leading edge could create large-scale effects. While these methods demonstrated vortex control was possible, most of them proved limited in the range of operating conditions in which they were effective.

On the trailing edge, Shih and Ding [80] applied the technique of particle image velocimetry (PIV) to quantitatively investigate the effect of a vectored trailing edge jet on vortex breakdown for both a static delta wing and a dynamically pitching wing. Vorobieff and Rockwell [81,82] attempted to optimize a leading edge flap and a variable trailing edge blowing actuation scheme by reducing the power inputs necessary to retard vortex breakdown on a pitching delta wing. All these techniques demand relatively power intensive systems and are not generally applicable to flapping wing flight.

5.3. Dynamic stall vortex control

The DSV arises when an airfoil stalls in an unsteady flow field. It commonly occurs when an airfoil oscillates in pitch near the static stall angle or it experiences large accelerations in pitch upward, as with military jets maneuvering at high angles of attack. Associated with the DSV are large detrimental changes in lift and moment coefficients from their nominal quasi-steady or steady-state values. The DSV represents a limiting operational condition for many rotorcraft and fixed wing aircraft operating at high AOA. Dynamic stall has also been identified as one of the major mechanisms in the development of the unsteady leading edge vortex [58]. Therefore, it is reasonable to assume that understanding dynamic stall and reviewing past efforts aimed at its control could aid in the creation of means to manipulate the same phenomena on flapping wings.

The most visible difference between dynamic and static stall is the emergence of a hysteresis in the C_L vs. α graph, as seen in Fig. 22. This strong hysteresis also

takes place in the moment coefficient, C_M vs. α curve. The hysteresis loop represents a transfer of energy to and from the airfoil to the freestream. If the sum of two sub-loops is negative, then there is a net transfer of energy from the freestream to the airfoil, resulting in an unbounded growth in the airfoil oscillations and in the extreme case, destruction of the airfoil. McCroskey [83] categorized the evolution of the DSV during one full cycle and described 11 distinct events during the process. Each cycle starts with the separation of a vortex at the leading edge and which then is convected downstream over the airfoil. This vortex, the DSV, causes the initial increase in lift, delays stall, and creates a large negative moment at the end of the cycle.

Since the initiation of the DSV is the same as for any other separating leading edge vortex, tangential blowing has also been successfully applied to delay the creation of the leading edge vortex. Alrefai and Acharya [84] applied leading edge suction from a slot positioned at 2% along the chord on the suction side of the airfoil to regulate the accumulation of reverse-flow fluid near the leading edge. More dramatic success, however, has been seen using a variety of leading edge devices. Carr and McAlister [85] and Yu et al. [86] found that a leading edge slat on VR-7 and VR-12 airfoils could control the DSV and considerably reduce the moment excursion and moderately shrink the lift hysteresis curve. Alexander [87] demonstrated far greater control by using a small leading edge oscillating fence, with the fence size set to 2% of the airfoil chord and the oscillation frequency corresponding to a Strouhal number of order one, both the DSV and boundary layer separation from the leading edge could be completely eliminated, causing an attendant reduction in the negative pitching moment. Prophet [88] expanded on this idea by using two fence type actuators to control the leading edge separation and the trailing edge stall phenomena. Optimizing the size, position, and oscillation frequency of the two fence actuators, he showed the elimination of the DSV, an 80% reduction of the negative pitching moment, a recovery of 50% of the nominal maximum C_L throughout the pitching cycle, and a complete collapse of the lift hysteresis.

5.4. Flutter

Flutter is a self-excited oscillatory aeroelastic instability of a structure caused by the interaction between structural vibrations and applied aerodynamic forces. This interaction draws energy from the flow field and transfers it to the lifting surface. It is of particular importance in any relatively high aspect ratio elastic structure exposed to unsteady flow, e.g., rotor blades in turbines, wings on passenger aircraft, and cable suspension bridges. If left unchecked, flutter vibrations can completely destroy the structure. In the case of flapping

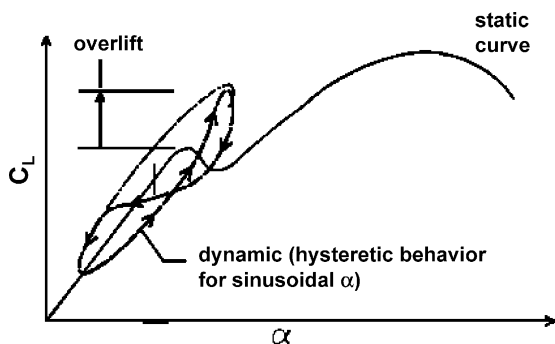


Fig. 22. Typical hysteresis loop for C_L vs. α for an airfoil in unsteady flow.

flight, the entire wing is flexible and flutter oscillations have not been seen to grow in time or size. The study of flutter, however, is important for flapping flight since it provides direct analytic tools to deal with the aeroelastic problem inherent in the flight of MAVs. Furthermore, knowledge gained from the study of flexible structures and unsteady airflows in MAVs can be transitioned back to more traditional flutter studies.

Classically, the flutter properties of a system are the lowest critical speed (U_F) and the associated reduced frequency (ω_F) for which a structure at a given density and temperature will sustain simple harmonic motion. Flight at U_F represents a neutral stability boundary, as all small structural oscillations must be stable below U_F . Above U_F , however, the small oscillations are not damped out and the structure is unstable for a range of speed (or at all speeds) above U_F . The calculation can be broken down into the following steps (after Bisplinghoff [89]):

- Determine the vibration modes of the structure with no aerodynamic forces present.
- Calculate the aerodynamic forces on the structure due to simple harmonic oscillations of the in vacuo normal modes as functions of speed and reduced frequency.
- Search for combinations of these parameters for which simple harmonic motion yields equilibrium between the structural inertial forces and the unsteady aerodynamic forces. These combinations are the flutter boundary.

In practice the calculation of (a) assumes that the vibration modes are a superposition of a finite number of preassigned mode shapes, i.e., all the vibrations are

linear. Torsion and bending can be coupled but all modes are linear. The aerodynamic force calculations in (b) generally assume some sort of linearized aerodynamic theory and hence do not capture the effect of flow separation, even though generally vortex flows such as the DSV can precipitate flutter.

5.4.1. Distributed piezoelectric actuators for flutter control

Lin et al. [90] demonstrated macroscale use of distributed actuator technology to solve aerodynamic problems. This group tested distributed piezoelectric actuators bonded onto NACA 66-012 airfoil with 30° sweep as a means to suppress flutter and increase the flutter speed, U_F . The test configuration is shown in Fig. 23. Piezoelectric actuators are strain actuators, in that application of a voltage across the piezoelectric material causes a large strain force to be exerted. Additionally, strain gauges and accelerometers were bonded to the wing and acted as local sensors. The results, however, showed that the control authority was limited due to saturation of the piezoelectric actuators. They believed increased coverage would improve the control authority. They did, however, increase the flutter dynamic pressure ($1/2\rho U_F^2$) by 12%.

5.5. MEMS for aerodynamic flow control

MEMS is an integrated circuit (IC) derived fabrication technology developed during the 1980s that enables large, batch scale production of micron scale mechanical devices, either as microactuators or microsensors. Some examples of MEMS products are micropressure sensors,

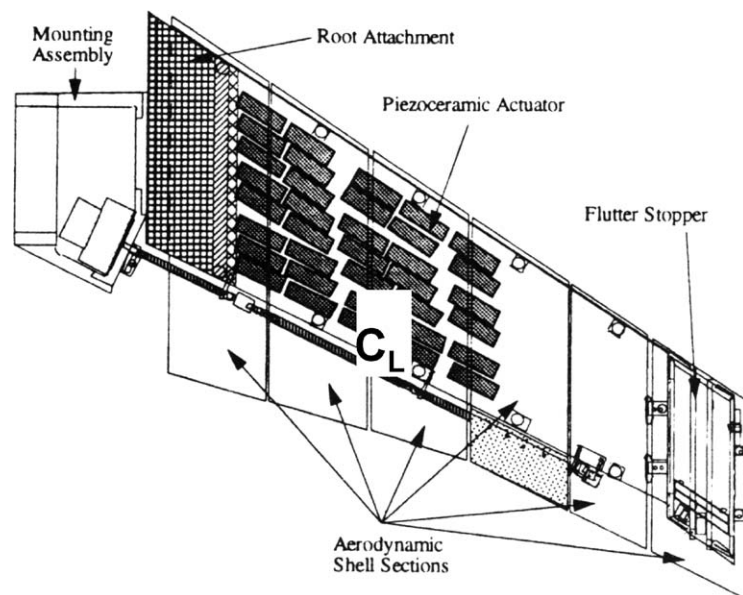


Fig. 23. Using distributed strain actuators to affect aerodynamic control. From Lin et al. [90].

accelerometers, inkjet printer heads, digital mirror devices for projection systems, optical switches, and lab-on-a-chip systems for separation, preparation, and detection of DNA or pathogens. Additionally, since the same processes are often used to create both MEMS devices and traditional IC circuits, by carefully designing the fabrication process flow it becomes possible to integrate transducers and microelectronics on the same wafer chip. This normally results in both cost savings and better performance.

Basic MEMS fabrication techniques include bulk micromachining, surface micromachining, and wafer bonding. Detailed information regarding the different techniques can be found in many textbooks (see especially the comprehensive texts by Madou [91] and Kovacs [92]) and review literature. Bulk and surface micromachining of silicon currently dominates in the fabrication of MEMS devices. A brief introduction of surface micromachining will be given here, as it will be used in the fabrication of some of the actuators and wings seen later.

Surface micromachining differs from bulk micromachining in that instead of etching devices out of the wafer substrate, it makes devices through the use of additive layers. Surface micromachining creates structures by depositing thin films on a substrate (commonly via techniques such as chemical vapor deposition, sputtering, or evaporation) and then selectively removing the unwanted parts, or sacrificial layers, through etching, using either a dry etch (with reactive gas mixtures) or a wet liquid etchant. In this way, free standing and movable parts can be fabricated. An example of a surface micromachined structure is shown in Fig. 24.

The development of MEMS technology has added vast new areas of exploration to fluid mechanics. Ho and Tai [93,94] provide a good review of MEMS applications in fluid mechanics. It spawned the new field of microfluidics, where the research ranges from new inkjet printer head designs to micromixers and microseparators for biomedical applications. Other examples of

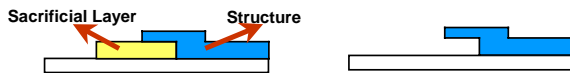


Fig. 24. Surface Micromachining.

MEMS fluidic sensors now available include piezo-resistive pressure sensors, shear stress sensors, and micromachined hotwires. In aerodynamics, flexible MEMS bubble actuators have been used to affect the rolling moment of a delta wing [79]. Flexible shear stress sensors have also been used to detect the separation line on a rounded leading edge of a delta wing as well as on a cylinder [95]. MEMS actuators are known to be relatively power thrifty and can interact with and manipulate the relevant flow structures to effect global flow property changes from local actuation. This ability is due to the length scale of the actuator (anywhere from hundreds of microns to a few millimeters) being comparable to the flow structure, thus allowing the actuator to directly excite flow instabilities at their origin. A distributed field of such actuators can therefore efficiently achieve large aerodynamic performance improvements. Of equal importance is also the ability to batch fabricate these devices on thin films and distribute them on the aerodynamic surface of interest to form a distributed control system.

5.6. MEMS electrostatic check-valve actuators

Although the dominant material in MEMS is silicon and the majority of fabrication techniques involve it, many other substances have been tested and incorporated into MEMS devices. Recently, there has been an emphasis on micromachining devices using “soft” materials such as polymers due to the interest in meshing MEMS with biological systems. Such hybrid systems require the use of biocompatible materials. One such biocompatible material is parylene, which has been used to fabricate a variety of valves and pumps for microfluidic applications. For flapping MAVs, parylene has been used both to form the wing membrane (which is typically only 20 μm thick) and as the structural material for electrostatically activated check-valves. Since parylene is used both as the wing membrane and check-valve material, these MEMS devices can be integrated directly on the wing, forming a complete unit that can be batch fabricated for mass production.

MEMS wings integrated with an active check-valve electrostatic actuator parylene skin are shown in Fig. 25 and close up photographs of the actuators individually and in array format are seen in Fig. 26. The check-valves



Fig. 25. Wing with integrated MEMS check-valve electrostatic actuators.

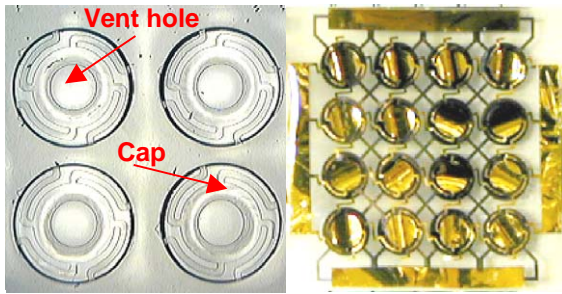


Fig. 26. Detailed view of check-valves (left) and in actuator array. Each actuator is approximately 1 mm^2 .

feature vented through holes with tethered parylene caps on the skin to rectify the airflow in one direction. Each vent hole is covered by a tethered valve-cap with a diameter of 500 and $900 \mu\text{m}$, respectively. Two metal layers are added for ground and high voltage contacts to form to electrodes, which will attract each other under an applied voltage. These contact pads are sandwiched in between two parylene layers and the entire assembly is less than $20 \mu\text{m}$ thick.

The electrostatic force, F_e , between two conductive plates with area A , separated by a gap d , and under an applied voltage V is given by

$$F_e = \frac{\epsilon_0 A V^2}{2d}, \quad (17)$$

where ϵ_0 is the permittivity of free space. Before being integrated on the wing, the actuators were successfully operated at 50 V, but after integration the operating voltages were 350 V. This was because the gap distance between the electrodes increased during the integration process. Since the force is proportional to V^2/d^2 , the voltage must be raised by its square to maintain the same force as the gap size increases. Lowering the operating voltage requires careful fabrication in order to reduce the electrode gap during the integration process. Details of the fabrication process and means of reducing the gap can be found in previous articles such as Liger et al. [96] and Pornsinsirak [97].

The actuators were placed near the leading edge where the perturbation of the flow can lead to significant aerodynamic effect, as was shown in control of the leading edge vortex over delta wings. The check-valve actuators are mounted such that they are closed during the downstroke and open on the upstroke when not powered. When powered, they remain closed during the upstroke. All the actuators are wired to turn on or off in unison, effectively making them a single actuator. There are approximately five sets of 16 check-valves per wing, resulting in a maximum of 80 check-valves per wing. The wings have a 7 cm span and 3 cm chord.

As shown in Fig. 27, the maximum lift peak occurs at the beginning of the downstroke (0–0.5) while the next

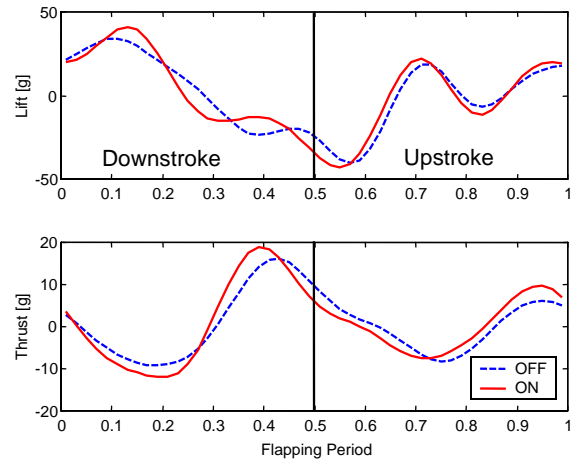


Fig. 27. Phased averaged lift and thrust for integrated MEMS check-valve wing. $J = 0.48$.

Table 1

Mean lift and thrust for cambered active-valve integrated MEMS wing

	ON	OFF	% change
Lift (g)	0.63	0.48	+ 31
Thrust (g)	1.17	1.00	+ 17

lower peak is near the middle of the upstroke (0.5–1.0). The vortex that forms underneath the wing during beginning of the upstroke contributes to the negative lift portion. Similarly, the results show that the maximum thrust is not produced until almost at the end of the downstroke which is the time when the flexible trailing edge begins to snap down. It is also the time when the separation vortex is being shed.

Observing Fig. 27, the actuator effect is seen from the plots of lift and thrust. The highest lift and thrust peak values (approximately 40 and 20 g, respectively) occurred when the actuators were turned on. When the actuators are 'ON' both lift and thrust differ up to 50% at a given instant in time in comparison to the 'OFF' value, which clearly indicates the effect of the valve. The valves *locally* manipulated the unsteady leading-edge vortex and changed the pressure distribution on the wings. It was also observed that as J decreases, i.e., flow unsteadiness rises, lift and thrust rose due to growth in the size and strength of the vortex, allowing the actuators to become more effective.

There were correspondingly large average percentage changes over one flapping cycle, as seen in Table 1. There was a 31% increase in mean lift and a 17% boost in mean thrust over the nonactuated wing. Interestingly, these gains came from pure actuation without any sort of feedback control loop in place and with digital

(on-off) type actuators. It would be interesting in the future to explore the effect of feedback control and more analog type actuators (half on, full on, full off, etc.) to see if even more improvement can be achieved.

6. Active flow control techniques and flapping flight

Quite a few reasons exist for why flapping flight could benefit greatly from an active, i.e., closed loop, flow control system. As seen in the previous section, open loop flow control performs well when the operating conditions are carefully restricted to the range within which the control mechanisms were designed. But outside the lab the operating environment can vary considerably from one instant to the next due to environmental factors such as a gust or wind or even due to mechanical damage to the wings themselves. Therefore, an active control system is needed to compensate for a wide range of flight conditions. Also, specifications for increased maneuverability call for an adaptive control technology that can intelligently alter the wing shape in order to generate adequate lift to meet the lowered wing loading requirement. Additionally, mechanical wings currently cannot effectively imitate the full range of motion and control displayed by natural wings and so it is no surprise that mechanical wings suffer in terms of performance compared to their biological counterparts. There are no muscles, feathers, or bone structure in mechanical wings comparable to those found in bird or bat wings. Active flow control therefore is a key component in closing the performance gap between the two without having to fully mimic the biological flapping motion, and hence reducing the mechanical complexity of the system. Essentially, satisfactory wing performance beyond the limited and narrow design range drives the demand for active flow control of flapping wings.

The major challenges of active flow control development largely center on an appropriate control system which can properly handle the complexity of the aeroelastic problem at hand. Previous sections have described the difficulties in aeroelastic analysis of the flexible flapping wing system. In the parlance of dynamic control engineers, the “plant”, i.e., the flapping wing complete with sensors and actuators, is a highly nonlinear system and there seems to be no linear control law or even an appropriate linear approximation. An active wing will, by definition, have many variable parameters, e.g., camber, stiffness distribution, twist, kinematical limitations, and this leads to a large state space for optimization. For example, if only 10 actuators with 5 states apiece are on the wing, then almost 10 million combinations are possible! This staggering number of states creates quite an optimization and control problem.

This section starts with an overview of closed loop linear control schemes. Then it quickly moves to nontraditional control algorithms such as genetic algorithms and neural nets and reviews their past application in a variety of active flow control experiments. Next, the Gur Game, a new nonlinear control algorithm, will be described. The Gur Game is especially appropriate for a distributed system of actuators operating in a nonlinear system. Some experimental results using this new controller in optimizing wing kinematics then follows.

6.1. Closed loop control of separated flows

Linear optimal control of flutter comprises the vast majority of work on closed loop separated flow control. This was largely due to the ease of analytically modeling and predicting linear systems with the limited computing technology available at the time. If the systems were inherently nonlinear, “reasonable” linearizing assumptions were made for either the fluid or structural mechanics models. While this approach has worked satisfactorily for many years, the recent requirements of supermaneuverability and the advent of active materials (particularly piezoelectric transducers and MEMS fluid sensors and actuators) now invalidate the old assumptions of attached flow, small wing deformations, and static material properties. Fortunately, the explosive growth of computing power has made possible the exploration of more computationally intensive control algorithms, such as genetic algorithms and artificial neural networks (ANNs). First, however, we start with linear control algorithms.

6.2. Linear quadratic (LQ) controllers for flutter suppression

The vast majority of closed loop control systems apply linear optimal control theory in order to produce a computable solution in terms of gain and phase margins. The use of LQ and linear quadratic Gaussian (LQG) controllers for active flutter suppression has a relatively long history. Theoretical work by Edwards et al. [98] considered an extension to the standard computation of flutter whereby the generalized unsteady aerodynamic loading was represented by a rational transform instead of a simple harmonic function. However, the transforms were still in the Laplace s -plane and hence the loading was still linear. In fact, it was derived from linearized aerodynamic theory using a 2-D airfoil. Newsom [99] followed the same path when he employed a Pade approximation to derive a deterministic LQ control law for flutter suppression using a trailing edge flap. Numerical simulations showed as much as 50% increase the dynamic flutter pressure, but again the model linearized aerodynamic loading with relatively small wing deformations.

Experimentally, Mahesh et al. [100] studied LQG control on a swept back wing with an active control surface. After calculating a high order LQG controller using linear aeroelastic theory with assumed simple harmonic steady-state wing motion, the group compared the use of residualization and frequency response matching to achieve lower order controllers. They found improvement in performance (adequate gain and phase margins), but it was only at one specific Mach number and they noted gain scheduling may be required for a range of Mach numbers. Mukhopadhyay [101] published results using LQG controller on a flexible wing with a trailing edge flap actuator and surface mounted accelerometers. After control law synthesis and order reduction of the controller, the closed loop controller increased the flutter pressure by 23% over the uncontrolled case. But he noted that discrepancies arose between the analytical and experimental frequency response for the actuator, which he attributed to the approximate modeling of the unsteady aerodynamics using attached flow when in fact, the flow may have separated. This points out the need for a viscous aerodynamic model that accounts for flow separation when dealing with flutter simulations. Finally, Lazarus et al. [102] used a LQG controller in conjunction with piezoelectric actuators to effect a change in flutter speed purely through changing the structural properties (namely the strain characteristics) of the wing. The result was an increase in flutter speed of 11%. This showed that a flap actuator was not needed to change the aerodynamic performance or flutter characteristics, but instead simple strain actuation could provide a means of extending the performance envelope.

6.3. Other linear controllers

Luton and Mook [103] conducted an interesting numerical study where they used linear feedback on the control of ailerons to suppress flutter on a nonlinear high aspect ratio wing undergoing large deflections. They employed unsteady vortex-lattice methods to model the flow, and so this model is not valid if the flow separates or if vortex bursting occurs. The simulation computed that the flutter divergence speed increased by almost 100%.

Frampton et al. [104] demonstrated the control of panel flutter with piezoelectric transducers, which acted as both sensors and actuators. Here they used linearized potential flow aerodynamics and calculated the response of a panel with an attached piezoelectric transducer mounted on the surface. The control law for the transducer used collocated direct rate feedback, in which a voltage input signal proportional to the sensed structural velocity was sent to the piezoelectric actuator. Stability was achieved for a limited range of transonic and supersonic flows, but they noted that actuator

saturation limited the amount of which this system could be stabilized.

6.4. Proportional integral derivative control of separated flows

Gursul et al. [105] changed the sweep angle of the delta wing to control vortex breakdown location. An integral feedback controller sought to minimize the rms value of pressure fluctuations induced by the helical mode instability found in vortex breakdown as a function of the sweep angle. This approach proved fruitful as the amplitude of the pressure fluctuation monotonically varies with the vortex breakdown location, thus making a simple first-order feedback control system possible. However, it is certainly not energetically efficient.

6.5. Genetic algorithm optimization

Genetic algorithms are evolutionary approaches to optimization, whereby a suitable representative sample of a given optimization space are chosen and measured against a 'fitness' measure. The specimens best matching the fitness measure are randomly mutated and then combined with other fit specimens. These new specimens, the offspring, are tested against the fitness measure. Then the best specimens from the original and new offspring sets are kept and the process starts again. Relatively little work has been published on the application of genetic algorithm optimization routines to controlling separated flows. One notable exception is by Milano et al. [106,107], who conducted a CFD study using a Controlled Random Search genetic algorithm to optimize the placement and operating parameters of two actuator systems (rotating surface belts and jet actuators) on a cylinder at low Re ($Re = 500$ and 1000 , respectively) in order to reduce the drag coefficient. The optimized cases showed over 50% drag reduction. However, it took up to 1500 iterations to converge, resulting in an expenditure of 30 h of CPU time on a NEC SX-4 supercomputer, making it computationally very intensive.

6.6. Neural network control of separated flow

Neural networks offer intriguing possibilities for closed loop control. Neural networks have been shown to be able to predict the behavior of nonlinear systems, recognize patterns, and optimize system behavior even in the face of uncertainty. Briefly, a neural network consists of an input layer with a number of different inputs, one or more 'hidden' layers where the weights are set, and an output layer, as depicted in Fig. 28. The hidden layers perform the real work, as they contain the weights, which determine whether a specific pattern is

recognized as a match or not. Training a neural network consists of feeding in an input set, setting the weights in the hidden layers, and seeing if the predicted output matches the known output. An error is calculated from any discrepancy and feed back into the hidden layer, where a backpropagation scheme adjusts the weights. This process continues until the predicted output matches the known output to within a specified tolerance.

Faller et al. [108] presents one of the few studies of closed loop control systems endeavoring to fully capture the inherent nonlinearities of three-dimensional unsteady separated flow fields. Building on previous work, they developed an ANN feedback controller capable of predicting the unsteady surface pressure topologies on a rectangular planform airfoil with NACA 0015 cross

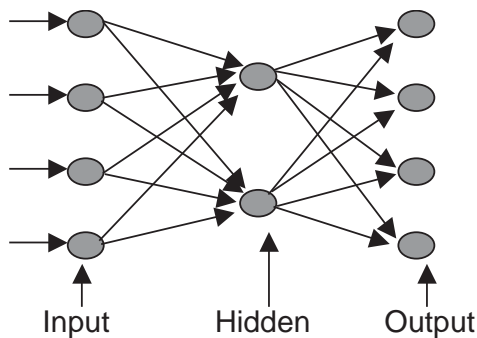


Fig. 28. A generic neural network.

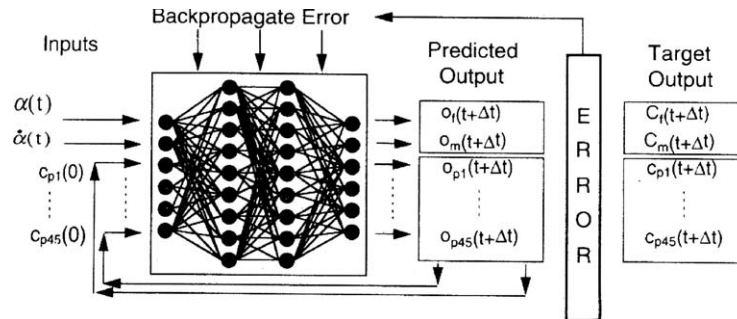


Fig. 29. ANN training process. From Faller et al. [108].

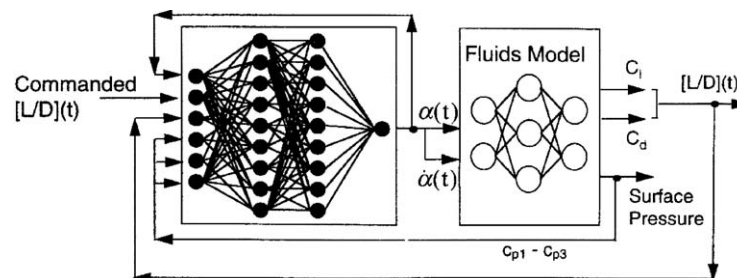


Fig. 30. ANN controller schematic. From Faller et al. [108].

section undergoing dynamic pitching. After training the ANN on several sets of data combining time-dependent surface pressure topologies and pitching motion history, they tested the control system in two ways. First, given a set of wing motion histories, the ANN was told to predict the resulting flow field and create a composite motion history (instantaneous AOA and angular velocity) that optimized lift/drag over the specified time interval, $[L/D](t)$. Secondly, a $[L/D](t)$ was given and the ANN was to create the motion history necessary to replicate the specified $[L/D](t)$. The neural net training algorithm is shown in Fig. 29 and the controller model shown in Fig. 30.

The results are rather impressive. The ANN accurately predicted the unsteady surface pressure distributions for motion histories on which it was not trained, as seen in Fig. 31. It also successfully created a motion history that optimized $[L/D](t)$ and solved the inverse problem, namely given a $[L/D](t)$, it produced the necessary motion history.

6.7. Angular speed control

Returning to the biological motivation for flapping MAV flight, it was noted earlier that birds are not limited to fixed wing kinematic motion, but instead change their wing motion to gain the most advantageous geometry during maneuver or transition from one flight mode to another. Although mechanical flappers do not have as large a range of motion in terms of number of

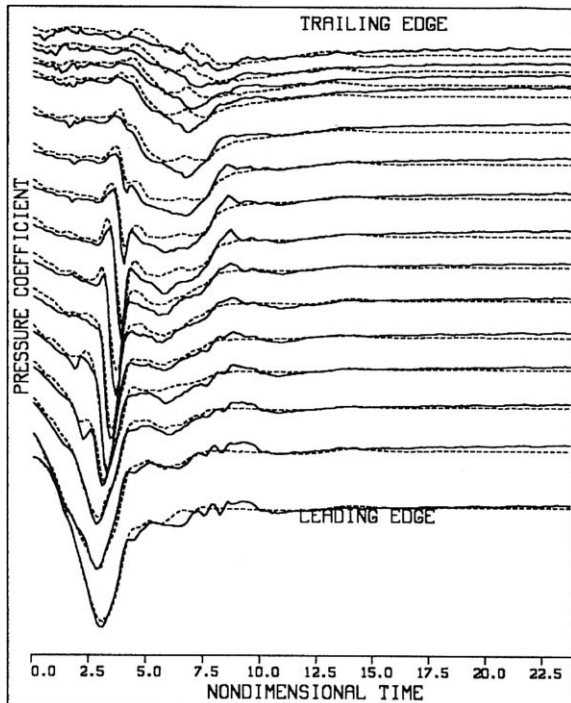


Fig. 31. ANN prediction of surface pressure distribution on an unseen case. The solid lines are the experimental data and the dotted lines the predicted values. Each line represents a different sensor location. From Faller et al. [108].

degrees of freedom, perhaps simple feedback adjustment of the wing motion could achieve similar results as for natural fliers. The simplest situation where variable wing kinematics could be applied is one in which the wings are driven by a rotary DC motor connected to a gearing system, as pictured in Fig. 32. By varying the drive signal to the DC motor, the angular speed of the wingtip will also vary in time. This change in wing velocity will cause changes in the growth and shedding of the unsteady leading edge vortex over the entire wing, i.e., global vortex control is possible by simply altering the DC motor drive signal and the instantaneous angular speed of the wing.

6.7.1. Experimental setup

The work was conducted in a small wind tunnel facility at the University of California, Los Angeles. The tunnel test section measured $30 \times 30 \times 60$ cm and had an inlet contraction ratio of 4:1. The speed range in the tunnel was 0–10 m/s, with most experiments being conducted between 3 and 4 m/s. The flow uniformity over the entire speed range of the tunnel was found to be 0.5%. The test section was modified to allow for smoke wire visualization using an 80 μ m diameter chromium wire that was electrically heated with 3 A. A mixture of



Fig. 32. DC motor and transmission system to flap wings.

mineral oil and aluminum powder periodically dripped on the wire to produce the smoke. Due to flow cooling of the wire, visualization was possible at speeds at or below 1 m/s. Load cells of 150 and 100 g capacity took unsteady force measurements of lift and drag, respectively. A 16-bit resolution ADC board allowed for minimum force resolution measurements of 33 mg for lift and 24 mg for drag. The ADC board had two analog output channels that powered the load cells and the dc motor on the test mount. A specially written LabView 5.0 routine automated the entire setup. Fig. 33 shows the experimental setup.

In order to perform the aerodynamic tests, a simple, lightweight flapping device had to be designed and built. The flapping cycle is intimately linked to the transmission design, and often it does not mimic the natural cases of bird or insect wing motion. The transmission (see Fig. 34) allowed for variation of a number of parameters that controlled the kinematic motion of the wing, namely: the total flapping angle, Φ ; the flapping frequency, ω ; the mean AOA, α ; the stroke plane inclination (the plane in which the flapping motion occurs); and the feathering angle, (the angle between the wing chord line and the stroke plane). The total flapping angle could be set to 60° or 90° . The feathering angle could be varied by rotating the wing about its shaft and tightening a set screw.

During the tests, a 6 mm diameter Namiki electric vibrator motor drove the transmission. The motor nominal voltage was 1.3 V with a stall torque of 0.8 g cm. The motor operated at up to 6 V and geared 24:1 to provide sufficient torque to drive the wings. With this motor the maximum flapping frequency was 15 Hz for the 90° flapper and 30 Hz for the 60° flapper. For the majority of tests, $\omega = 20$ Hz, $\Phi = 60^\circ$, the stroke plane was set perpendicular to the AOA, and the feathering angle was 0° . The normal flapping motion, which occurred when a constant voltage controlled the motor,

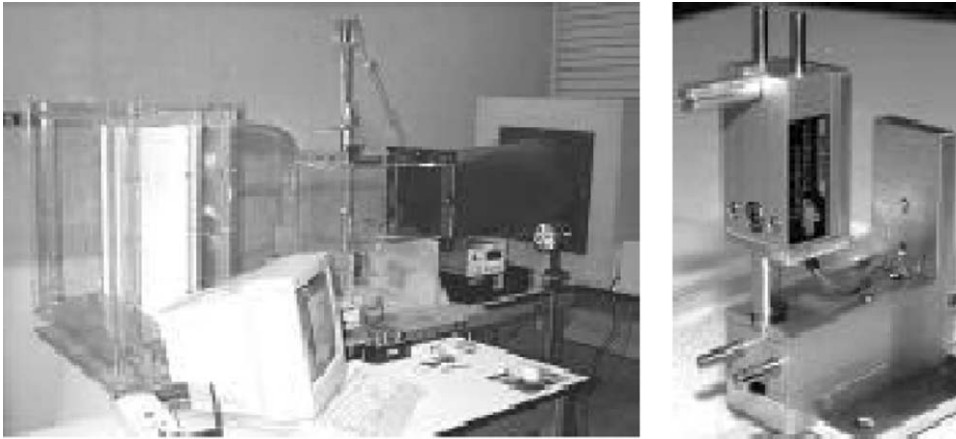


Fig. 33. Wind tunnel and test stand load cells.

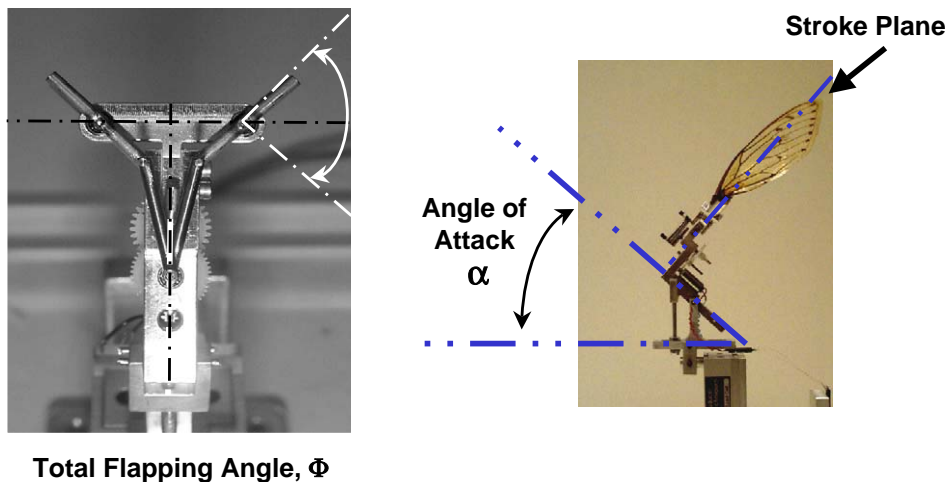


Fig. 34. Flapping wing parameters and transmission.

was sinusoidal in nature, with the result that the wing spent equal time in the upstroke and downstroke. The wingtips during this normal flapping motion traced an arc with a total angle of 60° and oscillated with a frequency set by the drive voltage.

6.7.2. Gur Game feedback control

Although angular speed control in its simplest form does not require the use of a nonlinear feedback controller, incorporating such a controller does have some advantages for this system. First, it is relatively easy to understand the operation of the control algorithm and map its limit using a simple actuator scheme. Second, once that is understood, it should be a straightforward extension to add a net of distributed actuators, such as MEMS devices, to the system. The addition of distributed actuators greatly complicates the analysis since it is difficult if not impossible to separate the effect of individual actuators at discrete locations

from the actuator set and the feedback controller as a whole. Therefore, it is desirable to first ensure that the feedback algorithm functions relatively well with less complex actuation schemes.

With the actuation system set, the closed loop control system must be able to both handle and optimize a highly nonlinear plant and a distributed actuator field while maintaining robustness in the flight performance of the vehicle under uncertain and time varying conditions, such as actuator failure or environmental changes. It should be no surprise there exist very few control schemes capable of this task. Most feedback controllers require either a linear plant, a small number of actuators, full state information, time invariance, or some combination of these factors. The Gur Game controller was designed specifically for distributed systems acting in a nonlinear, time varying environment and it should prove robust to random changes in operating conditions or actuator failure.

Much like a genetic algorithm or neural net control algorithm, the Gur Game aims for self-organization and self-optimization of the system [109,110]. The essence of the Gur Game is a random walk that is strongly biased toward the global optimum. The key concept in the Gur Game is the global figure of merit, called the reward function, which measures the performance of the system as a whole. The reward function maps the system state from 0 to 1, with higher system performance corresponding to values nearer to 1. At each iteration through the control loop, the reward function is evaluated. Then each actuator is changed probabilistically according to the reward function value. For example, suppose there are two actuators and the reward function value is 0.7. Then for each actuator a random uniform number from 0 to 1 is chosen and compared to the value of the reward function. If the random number is less than the value (0.7 in this case), the actuator changes state in a prescribed manner. If it is greater than 0.7, the actuator remains in the same state. This process is repeated for each actuator during each iteration. Eventually a global optimal state is achieved.

More formally, consider a finite state automaton with two outputs, A_0 or A_1 . At each discrete time t , a reward probability $r_0 = r(A_0)$ or $r_1 = r(A_1)$ is generated, depending on the output at time t and assuming $r = r_0, r_1 \in [0,1]$. As before, with probability r the automaton is rewarded; with probability $1 - r$, it is penalized. At the next time $t + 1$, the cycle repeats: the automaton chooses either A_0 or A_1 to output, a reward probability is determined, and the automaton is rewarded or penalized. The question now becomes how well does this automata perform to maximize the reward in relation to another automata that simply randomly chooses from A_0 or A_1 with probability $\frac{1}{2}$?

To answer this question, Tsetlin [111] developed the following automata design. Let the automaton have two states, -1 and 1 . If the state is -1 , the automaton chooses A_0 ; if it is 1 , it chooses A_1 . If the automaton is rewarded, it stays in the same state. Otherwise, it moves to the other state. Clearly, this will push the automaton toward behavior producing a reward.

The automaton's steady-state behavior can be modeled as a Markov chain where the transition probabilities from one state to another are exactly the reward probabilities. Defining $\pi_i (i = -1, 1)$ as the steady-state probability of being in state i . Now assume that $r_0 = 0.4$ and $r_1 = 0.8$. Equating the transition probabilities leads to

$$\pi_1(1 - r_1) = \pi_{-1}(1 - r_0), \quad (18)$$

$$\pi_1 + \pi_{-1} = 1. \quad (19)$$

This gives $\pi_1 = 0.75$ and $\pi_{-1} = 0.25$, i.e., the automata chooses the higher reward state three times more often than the low reward state. This translates to an

average reward probability of 0.7, compared to only 0.6 when the automaton chooses randomly between A_0 and A_1 .

For better performance, the automaton can have more than two states. Suppose it has $2n$ state, $S_n = \{i, -i | 1 \leq i \leq n\}$. This automaton is then said to have a memory size n . If the current state is negative, its output is A_0 ; if it is positive, the output is A_1 . Now, if a reward is received, the automaton stays in state n or $-n$ if it is in either one of those states. Otherwise it moves from state i to $i + 1$ if i is positive or from i to $i - 1$ if i is negative. For a penalty, if it moves from state 1 to -1 or vice versa it is at the extreme ends of the state space, otherwise it moves from state i to $i - 1$ if i is positive, or from i to $i + 1$ if i is negative. The effect of all this is to move toward the center of the state space if penalized, and away from the center if rewarded.

Although more complicated, the Markov chain analysis of the behavior still applies.

Tung [109,110] solved for the probability of being in state A_1 and found:

$$\Pr(A_1) = \sum_{i=1}^n \pi_i = \frac{4^n - 1}{2 - 3(2/3)^n + 4^n}. \quad (20)$$

For $n = 1$, the probability is the same previously found, $\pi_1 = 0.75$. As $n \rightarrow \infty$, this probability goes to 1. In fact, for any r_0, r_1 , such that $r_1 > r_0$ and $r_1 > \frac{1}{2}$, the probability of choosing A_1 converges to 1 as $n \rightarrow \infty$; meaning that as the memory size increases, the automaton will choose the best option with increasing certainty. For the general case of N automata, this continues to hold true.

The advantages of the Gur Game are that it can achieve a globally optimal state with many distributed actuators without having to explicitly dictate the operation of each actuator. The actuators self-organize and self-optimize based on the reward function. The reward function can be virtually of any shape; multimodal, discontinuous, nonasymptotic, etc. This framework provides for a very general and robust distributed control method.

6.7.3. Open loop test results

Simple variation of the rotational speed of the DC motor that drove the wing flapping assembly achieved global control of the unsteady leading edge vortex over the entire wing. The DC motor operated in the linear regime (the wing flapping frequency increased linearly with voltage input to the motor) and there was no motor slip in this mode of operation. A constant DC input voltage created a constant wingtip velocity. By varying the motor input voltage, the instantaneous angular wingtip velocity is now free to accelerate or decelerate. In order to compare the results of changing the angular speed to the constant speed case, the flapping period

remained fixed. Hence, angular speed control really means the tailoring the relative downstroke and upstroke times. For example, the wing might beat faster on the downstroke and slower on the upstroke.

A MEMS (i.e., no integrated actuators) wing flapping at $J = 0.48$ was tested and Fig. 35 shows the phase average results while Table 2 lists the quantitative change in lift and thrust over one flapping period. In Fig. 35, OFF refers to constant DC voltage input and

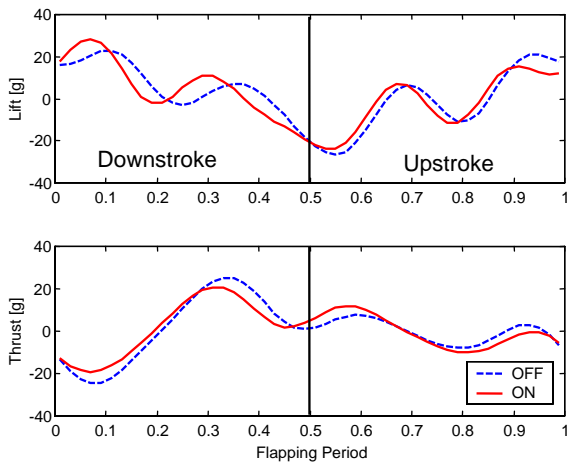


Fig. 35. Phase averaged lift and thrust for angular speed control of MEMS wing, $J = 0.48$.

Table 2
Mean lift and thrust for angular speed control of reference wing

	ON	OFF	% change
Lift (g)	1.78	1.94	−8
Thrust (g)	0.48	0.38	+26

ON means the drive signal was varied. In this test, the drive signal was a 20 Hz sine wave with an amplitude of 1 V and a DC offset equal to the constant DC voltage for the OFF case.

Table 2 shows that simple variation in the motor drive signal caused significant changes in the lift and thrust (−8% for lift and +26% for thrust). However, this system was not optimized and there was no feedback control.

6.7.4. Closed loop test results

The Gur Game controller was used in conjunction with the angular speed control concept as discussed previously (see Fig. 35). The reward function was based on increasing C_L/C_T . A square wave signal drove the DC motor and the signal was synchronized with the start of the downstroke by an external trigger. The transmission mechanism interrupted a laser beam and set the trigger. The amplitude and DC offset of the square wave were 1.0 and 4.8 V, respectively. The Gur Game controller, however, was free to change the duty cycle of the square wave from 0 to 0.6 in steps of 0.1. In this case, a value of 0.5 corresponded to 50% duty cycle. The controller turned on at $T = 20$ s and turned off at $T = 100$ s. The system state was measured every second. Simple titanium spar wings with parylene membranes operating at an advance ratio of $J = 0.6$ were tested.

As seen in Fig. 36, turning on the controller at $T = 20$ quickly increased the C_L/C_T and soon it reached a value of 3, which is greater than 300% of the non-controlled value of 0.8, and converged to a duty cycle value of 0.4. But because the Gur Game continually searched for new maxima, it changed the duty cycle and C_L/C_T plummeted, as observed around $T = 60$. The Gur Game then recovered the original optimal duty cycle and C_L/C_T again reaches 3 before the controller turned off at

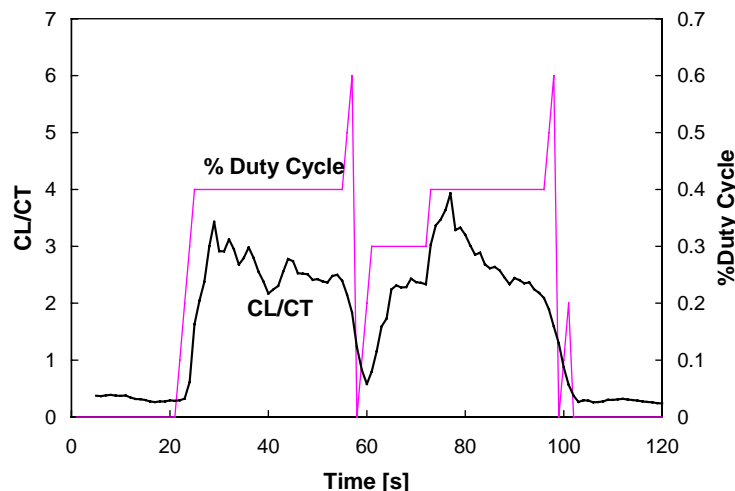


Fig. 36. Duty cycle optimization using the Gur Game controller and angular speed variation.

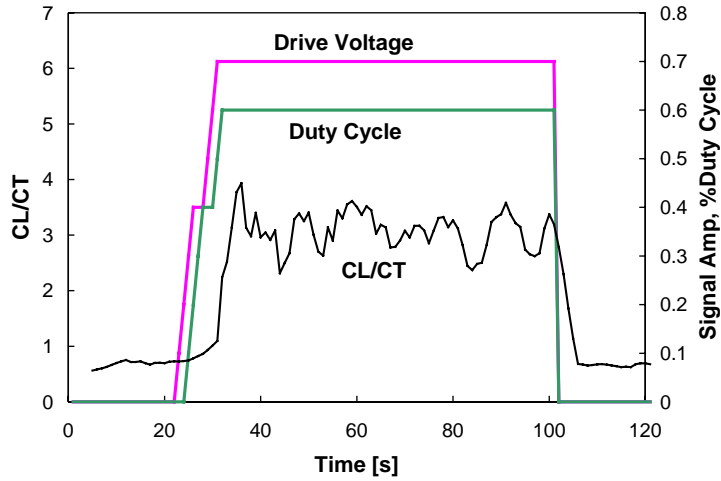


Fig. 37. Two variable optimization using the Gur Game controller and angular speed variation.

$T = 100$. This example demonstrated the robustness and search capabilities of the control scheme.

Tests of control and optimization for two variables were also conducted. Fig. 37 illustrates the results of optimizing both the duty cycle and signal amplitude of a square wave drive input. The experimental conditions were the same as for the previous case but this time both the amplitude of the signal and the duty cycle varied simultaneously. The signal amplitude ranged from 0 to 0.7 volts and the duty cycle went from 0 to 0.7 in steps of 0.1. Again, C_L/C_T was the reward function variable and the controller turned on at $T = 20$ and off at $T = 100$ s.

The controller again quickly converged on and remained at an optimal state of 0.7 for the signal amplitude and 0.6 for the duty cycle. The rise in C_L/C_T was 300%, and matched the best case achieved with single variable control and optimization.

These simple closed loop tests showed the ability of the Gur Game control algorithm to successfully optimize a highly nonlinear system without a detailed model of the plant. Although the actuators were limited in both scope and number, the controller is expandable to more parameters.

7. CFD model with integrated feedback control

CFD is a valuable tool to understand the fundamental physics of flapping wing flight. Direct computation of the full Navier–Stokes equations coupled with an appropriate FEM of the wing allows for a detailed view of the evolution in strength, size, and position of unsteady vortices, as well as their interaction with the deformation of the wing during the flapping cycle. This information is often not readily available via experimental methods. Furthermore, a feedback control algorithm can be integrated into the CFD model to

yield information on optimal wing shape, the effect of different actuation methods, actuator placement, and place an upper bound on wing performance. These studies could be very costly and time consuming to do experimentally. Hence, a CFD simulation can shorten the design and test cycle and its associated expenses.

The remainder of this section describes a model of the flapping wing that incorporated CFD, FEM, and the Gur Game feedback control algorithm into a single integrated simulation. The simulation solved for both the fully unsteady and three-dimensional flow field and featured explicit two-way aeroelastic coupling between the wing deformation and the flow solution. Further, the Gur Game algorithm evaluated the stiffness distribution of the wing and optimized wing stiffness to maximize both lift and thrust performance. By comparing the difference in wing stiffness of the original and optimized wing, the physical reasons underlying the gains in aerodynamic performance were extracted.

7.1. Flapping wing model description

The simulation used commercially available CFD software (CFD-ACE+ 2002) from CFDRC corporation. CFD-ACE+ provided a multi-disciplinary simulation environment and solved the Navier–Stokes equations in a Lagrangian–Eulerian reference frame. Specifically, it solved the continuity and momentum equations using a control volume approach:

$$\frac{d}{dt} \int_V \rho \, dV + \int_s (\rho(v - v_g) \cdot ds) = 0, \quad (21)$$

$$\frac{d}{dt} \int_V \rho \phi \, dV + \int_s \rho \phi (v - v_g) \cdot ds = \int_s q \, ds + \int_V S_\phi \, dV, \quad (22)$$

where ρ is the fluid density, ϕ are the Cartesian velocity components, v is the absolute fluid velocity, q the diffusive flux and S_ϕ the volume sources, \forall is the computational cell volume, S are bonding cell surfaces, and v_g is the grid velocity. As the grid moved with time, a space conservation law must be satisfied,

$$\frac{d}{dt} \int_{\forall} d\forall = \int v_g ds, \quad (23)$$

which ensured that the grid velocity balances the time rate of change of the computational cell volume. Failure to satisfy the space conservation law will introduce errors in the form of false mass sources into the solution.

To model the wing structure, CFD-ACE+ had a structural dynamics module, named FEMSTRESS. FEMSTRESS used the finite element method and solved the equation of motion

$$[M]\{\ddot{q}\} + [C]\{\dot{q}\} + [K]\{q\} = \{F\}, \quad (24)$$

where $\{q\}$ is the displacement vector, $[M]$ is the mass matrix, $[C]$ is the damping matrix, $[K]$ is the stiffness matrix, and $\{F\}$ is the force vector due to the fluid dynamic load and shear stresses.

This study used the two-way coupling feature of CFD-ACE+ and the FEMSTRESS module to accurately link the aerodynamics and structural dynamics. The FEM and flow solver operated in an iterative manner during each time step until the solution converged to within a prescribed difference. Normally, 10–20 iterations were required to ensure full satisfaction

of the fluid dynamics and structural dynamics solution within each time step.

7.1.1. Model validation

Fig. 38 depicts the three-dimensional computational domain developed for the flapping wing. The gridding was nonuniform, with cells more densely clustered near the wing and less densely packed near the inlet and outlets of the computational box. This captured the critical details of flow separation near the leading edge. An integration of the pressure field around the wing then yielded the total lift and thrust. The wing itself was $7\text{ cm} \times 3\text{ cm} \times 0.01\text{ mm}$ (span \times chord \times thickness) and sat inside a computational domain extending 13 cm in the spanwise direction from the wingtip, 21 cm in the chordwise direction from both the leading and trailing edges, and 21 cm above and below the wing. These boundaries were identical to the boundaries in the experimental apparatus. Fig. 39 shows the wing as modeled in the CFD code and compares it to the actual wing. The titanium spars had a Young's Modulus value of 110 GPa with a density of 4500 kg/m^3 while the parylene membrane had a Young's Modulus of 2.8 GPa and a density of 1289 kg/m^3 . To save computational effort, a symmetry plane was placed 4 cm from the chord which allowed modeling of only one wing.

A steady-state model of a wing with a rectangular platform at a fixed AOA and fixed freestream velocity was constructed to determine how many computational cells would typically be required to accurately capture lift and thrust performance. The CFD lift and thrust

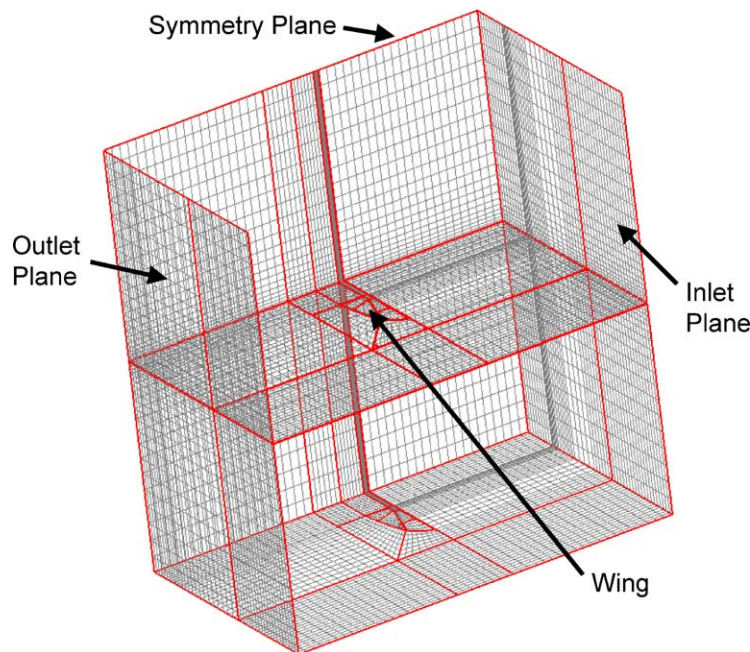


Fig. 38. Cut-away view of computational domain for flexible wing.

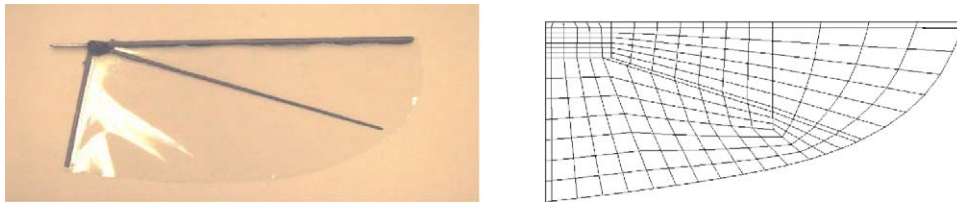


Fig. 39. Actual wing and CFD wing showing both spar and membrane.

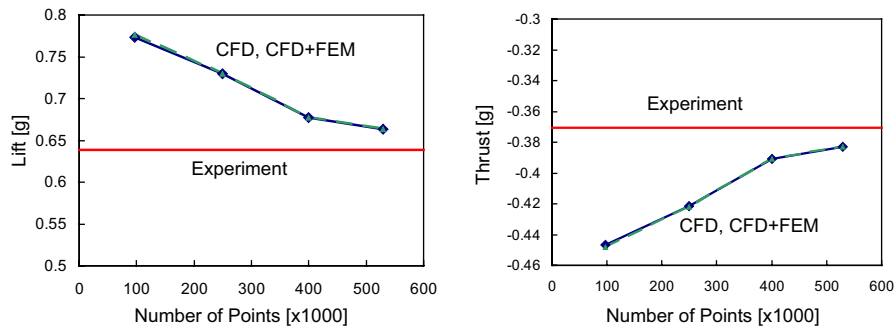


Fig. 40. Steady-state CFD validation.

results were then compared with experimental data taken in the wind tunnel on a same sized rectangular wing. This test provided a crucial validation step and yields important information on the trade off between grid resolution and computational run time in the model. The computational box of the rectangular wing was nearly identical to that of the curved flapping wing.

The test conditions were a freestream velocity of 1.7 m/s and a 30° AOA. The range of grid points from 97,000 to nearly 530,000 total cells were tested. The CFD model was run first with only the flow solver turned on, then rerun with the flow solver and FEMSTRESS module both on. This yielded an estimate of the error introduced by the FEMSTRESS solver. Fig. 40 shows the results of the simulation as a function of the number of grid points.

From Fig. 40 several items are apparent. First, as expected, the CFD model began to match the experimental model as the number of cells rises. The experimental data itself had a minimum resolution of 60 and 54 mg of force for the lift and thrust, respectively. Taking the uncertainty in the experimental results into consideration, a reasonable number of grid cells would seem to be approximately 500,000 cells. Rerunning the simulation for a 5° AOA and $U = 1.7$ m/s led to the computation matching the experiment within the experimental error at 100,000 cells, indicating that resolving large-scale flow separation requires many more cells than for smoothly attached flow. Finally, note that the addition of the FEMSTRESS solver affected the solution by less than 1%, indicating it was not a major source of computational error for this case.

After establishing the number of grid cells needed to resolve the lift and thrust components in steady-state flow and verifying the negligible errors introduced by the FEMSTRESS module, the model was validated in the unsteady flow regime. The model has been assessed against unsteady ($J = 0.6$) experimental conditions with both rigid membrane wings and flexible wings, as reported in detail by Ho [112]. In all cases, the kinematic parameters of the flapping wing (total flapping angle, AOA, flapping frequency, stroke plane inclination, and feathering angle) in the simulation were identical to the corresponding test cases taken from wind tunnel tests. These parameters were described in Section 6.7.1.

The wing membrane in both the simulation and the wind tunnel tests was initially flat. During the flapping cycle, the flexible membrane led to a great degree of wing deformation with a cyclic periodicity equal to the flapping frequency. During the entire downstroke cycle, the membrane remained relatively undeformed near the leading edge and the chord, but trailing edge exhibited an almost half period sinusoidal curvature with the peak residing near the tip of the diagonal spar. This portion of the trailing edge was elevated above the plane formed by the leading edge and chord. The deformation was not unlike that produced when one held a piece of paper by one corner and then blew air at the diagonally opposite corner. Accompanying the transition from downstroke to upstroke is an equally short and dramatic transition in the wing deformation. During this time, the curvature of the trailing edge reverses, starting near the leading edge and moving to the chord. The trailing edge near the diagonal spar now trails the motion of the leading

edge-chord plane and the wing deformation is nearly the opposite of what it was during the downstroke. Finally, during the transition from upstroke to downstroke, the trailing edge switches back to its earlier curvature and the cycle repeats.

Fig. 41 displays streamlines from the experiment taken using a smoke wire apparatus (selected streamlines have been highlighted) and compares them to the velocity field from the simulation for the same test conditions. Qualitatively, the two streamline fields match quite well. In Fig. 41(A) the growth of the separation bubble on the top surface of the wing is clear in both the experimental and computational images. The size of the separation bubble also appears to be of similar size in both snapshots, although the bubble sat closer to the leading edge in the CFD model. Fig. 41(B) shows that the separation bubble has completely enveloped the top of the wing by the end of the downstroke for both the experimental and CFD model.

As seen in Fig. 42, when comparing phase averaged force measurements over one flapping cycle, the lift curves agree very well while there was some discrepancy in the thrust production during the upstroke. Although the test conditions were only for $J = 0.6$ and $\alpha = 30^\circ$, the phase average agreement shown in Fig. 42 was representative of the agreement achieved for other conditions. The reason behind the discrepancy lies in the nonlinear nature of the aerodynamic and structural coupling. As noted previously, the structural deformation was intimately tied to the aerodynamic forces and the coupling was two-way. In the CFD model the wing

properties were known exactly but this was not true of the real wing. Minor variations in spar thickness, particularly along the diagonal spar, can lead to different deformations. The thrust production is especially sensitive to the wing deformation, as the shedding of the vortex off the trailing edge determines the thrust forces produced. Any variation in trailing edge deformation will dramatically affect the thrust. Overall, it was concluded that the CFD model offers satisfactory predictive capabilities for flexible wings operating in highly separated flows.

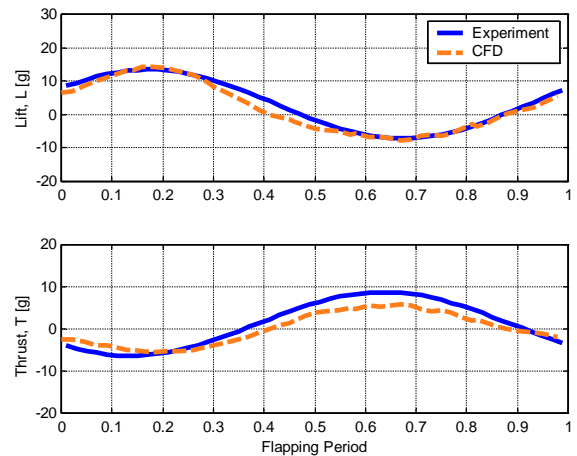


Fig. 42. Phase average lift and thrust comparison between CFD and wind tunnel tests.

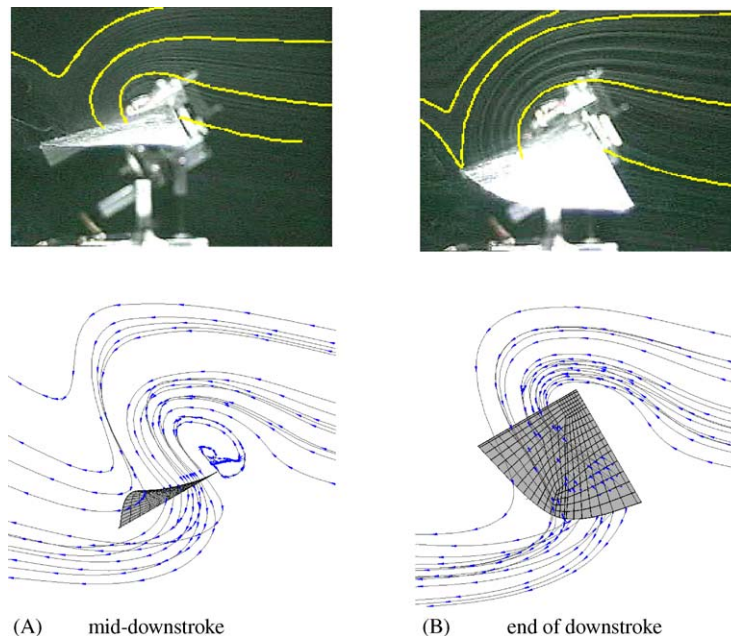


Fig. 41. Comparison of experimental and CFD streamlines.

7.2. Integrated distributed control algorithm model

A fully integrated simulation was created by combining a flexible wing, a set of actuators, and the Gur Game feedback controller. For greater generality and simplicity the simulation had a rectangular planform with 6 actuators distributed over wing, as seen in Fig. 43. The actuators manipulated the stiffness distribution by changing the local Young's Modulus. As noted previously, the aeroelastic response of the wing fixes the lift and thrust production as it directly affects the vortex evolution over the flapping cycle. Each actuator, denoted by E_n , had 6 possible states for the Young's Modulus, chosen from the set $S = \{1 \times 10^4, 5 \times 10^4, 1 \times 10^5, 5 \times 10^5, 1 \times 10^6, 5 \times 10^6, 1 \times 10^7, 5 \times 10^7\}$ Pascals. With 6 actuators, this led to $6^8 = 1,679,616$ possible states. The set $\{E_n\}$ was held constant over one flapping cycle.

The reward function was simply the magnitude of the force coefficients:

$$R = 2\sqrt{C_L^2 + C_T^2}. \quad (25)$$

If either C_L or C_T were negative, then the reward function returned zero. This disallowed wing configurations that did not meet the basic lift or thrust requirements for trim flight.

Fig. 44 shows the results of the rectangular wing with integrated controller simulation. The test conditions were $J = 0.6$ and $\alpha = 5^\circ$. At iteration 1 the algorithm starts with a rigid wing ($E = 5 \times 10^7$ Pa for all areas) producing a small amount of lift and thrust, ($C_L = 0.02$ and $C_T = 0.036$, respectively). Until approximately iteration 25, the controller discards a number of possible stiffness distributions, even though a few of them look promising with large increases in the thrust and lift coefficients. For example, at iteration 4, $C_L = 0.051$ and $C_T = 0.198$, or a 250% and 550% increases in lift and thrust, respectively. However, the resultant reward is only 0.41. Since the controller requires the reward to be equal to or greater than 0.5 for convergence, this wing configuration is not optimal. Indeed, one of the strengths of the Gur Game algorithm is that even seemingly large performance gains are not automatically judged to be optimal, but that the algorithm continually searches for better states. Near iteration 30 the

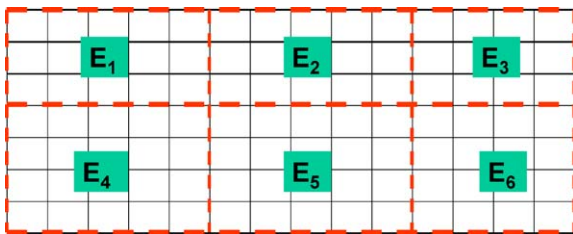


Fig. 43. Rectangular wing with distributed actuator field, E_n .

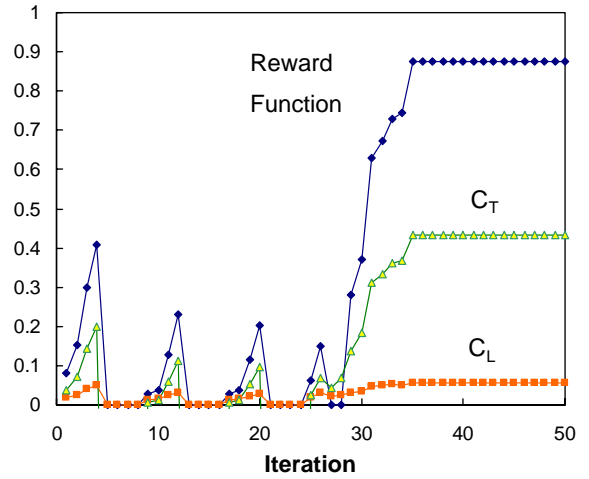


Fig. 44. System performance of the flexible wing and integrated controller simulation.

controller detects a very promising set of states and quickly converges onto an optimal state with $C_L = 0.056$ and $C_T = 0.434$, resulting in a reward value of $R = 0.875$. Notice that even though there were several states with $R > 0.5$ the controller did not get stuck in those intermediate states.

The final state for this case was $\{E_1 = 5 \times 10^4, E_2 = 5 \times 10^4, E_3 = 5 \times 10^5, E_4 = 1 \times 10^6, E_5 = 5 \times 10^4, \text{ and } E_6 = 5 \times 10^5\}$ Pascals. This corresponds roughly to a flexible membrane near the leading edge, although the leading edge was kept stiff due to a boundary condition on the motion of the leading edge required for numerical stability, and a stiffer membrane nearer the far tip of the membrane. Interestingly, this was also the same configuration found for the first generation of MEMS wings, where a diagonal spar was placed to stiffen the membrane at the outer portion near the tips. To achieve these gains required the membrane stiffness to be lowered by, on average, two orders of magnitude. Therefore, the membrane must be highly flexible and deformable to reach optimal performance. Again, this is the same conclusion reached from the experimental studies of natural, carbon fiber and mylar, and MEMS wings.

Physically, the increase in the reward function stems primarily from the rise in C_T , as clearly seen in Fig. 44. This is consistent with the realization in earlier sections that the wing stiffness distribution dramatically alters thrust more than lift due to the dependence of thrust on wing deformation and force generation, while lift relies on initial vortex generation at the leading edge, i.e., on the velocity and spatial motion of the leading edge. Therefore, for a given prescribed motion, changing the wing stiffness should alter the thrust much more than the lift. The simulations bears this out. Finally, repeating the simulation resulted in the convergence of the system, but at a number of slightly different reward values, i.e.,

slightly different wing stiffness distributions. These reward values were near 0.9, indicating that instead of only one optimal state, there exists a number of states that produce near optimal results. Optimizations run at high angles of attack, i.e., $\alpha = 30^\circ$ and 45° , produced similar gains in aerodynamic performance.

Another optimization modeled a MEMS wing (i.e., titanium spars and parylene membrane wing) with a 7 cm span and 4 cm chord, which is slightly larger than the wing described in Section 7.1. The optimization was run at $J = 0.6$, $\alpha = 30^\circ$. Fig. 45 depicts the MEMS wing and the areas on the wing membrane representing the stiffness actuators.

Fig. 46 graphs the results of the optimization. Starting with a rigid base wing and a $C_L = 2.15$ and $C_T = -0.1$, the wing quickly reached a near optimal state after only a few iterations. However, the Gur Game controller continued its search and managed to “fall over the cliff” by reducing the wing stiffness to such a point that the flow solver diverged, resulting in a zero reward value. It continued changing the membrane stiffness and eventually managed to refine the optimal states, where it stayed for the remainder of the run. After the optimization, $C_L = 2.38$ and $C_T = 0.36$ or a nearly a 11% and 460% rise in lift and thrust, respectively.

7.3. Physical mechanisms

The first step to understanding why flexible rectangular wing found by the Gur Game algorithm outperforms the original rigid rectangular wing lies in examining the phase averaged lift and thrust curves of the two wings, as seen in Fig. 47. The test conditions were $J = 0.6$ and $\alpha = 30^\circ$. Focusing on the downstroke (between 0 and 0.5 of the flapping period), it is very surprising to see that while the lift curves are similar for the two wings, the thrust curves differ dramatically, with the flexible wing producing much less negative thrust, i.e., lower drag, than the rigid wing. This happens over most of the downstroke and is not confined to a small portion of the sub-cycle. Another surprise awaits on the upstroke (0.5–1.0 of the period), where now the

instantaneous thrust forces are alike but the lift forces are not. During the upstroke the flexible wing creates less negative lift than the rigid wing. The conclusion is

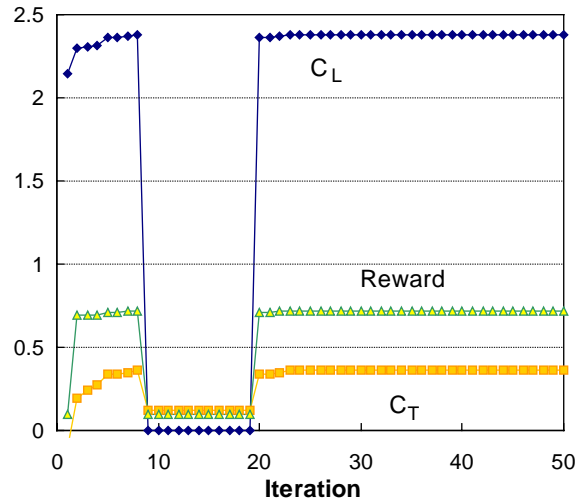


Fig. 46. MEMS wing optimization.

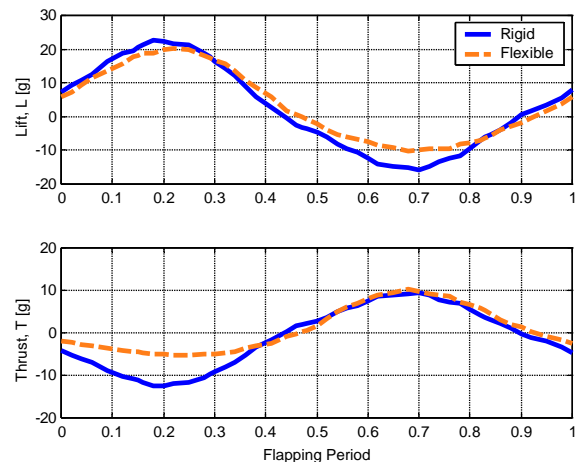


Fig. 47. Phase average performance of rigid and flexible wings.

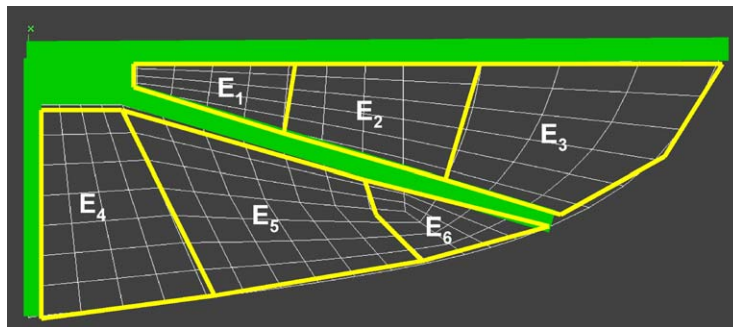


Fig. 45. MEMS wing with optimization areas defined.

then that the flexible wing does not outperform the rigid wing by increasing the positive lift and thrust forces, but by reducing the negative forces over the flapping period.

The focus now shifts to what physically occurs as the wing flaps to produce this unexpected conclusion. Since vortices dominate the flow field, viewing the evolution of vorticity through the flapping cycle might provide a global view of the physical processes involved in overall force generation.

Fig. 48 captures the vorticity production and shedding at key points during the flapping period for both wings. They show a slice of the vorticity field taken at the mid-span. The vorticity was normalized and mapped from -1 to 1 . The wing is viewed from the side. At the start of the downstroke (Figs. 48(a) and (b)), a large vortex from the preceding upstroke sits underneath the leading edge, and a trailing edge vortex wake of almost four chord

lengths in size remains behind both wings. By the middle of the downstroke (pictured in Figs. 48(c) and (d)), the unsteady leading edge vortex takes coherent form and the trailing edge vortex wake has now flipped to the upper trailing edge surface. For the rigid wing, the vortex wake appears almost perpendicular to the trailing edge, while the flexible wing creates a wake that tilts away from the trailing edge. Next, Figs. 48(e) and (f) illustrate the vorticity at the downstroke to upstroke transition. The trailing edge vortex has nearly finished shedding during the downstroke of the rigid wing and only a weak vortex remains in the wake behind the wing. On the other hand, the flexible wing only starts to shed the trailing edge vortex and we see a strong vortex ready to separate from the trailing edge vortex. In the last series of picture, Figs. 48(g) and (h), the trailing wake again flips over the trailing edge and now appears on the underside of the wings. The rigid wing has almost no vorticity about the wing on the upstroke, since it shed the trailing edge vortex earlier on the downstroke and the shed vortex has already dissipated. The flexible wing, meanwhile, still sees the remnants of the trailing edge vortex shed during the downstroke to upstroke transition. This wake also dissipates by the time the wing reaches the end of the upstroke. In both cases at mid-upstroke, a strong vortex resides underneath the leading edge, representing the negative lift component in the phase average force measurements.

While very descriptive and illustrative of the physical processes involved in flapping flight, the vorticity evolution and streamlines by themselves do not directly answer the question of why the flexible wing acts differently than the rigid wing. To fully understand the root causes requires finding which areas of the wing bear responsibility for the performance divergence and then closely analyzing the flow structure and wing deformation in those areas.

As found by Ho [112], mapping the total lift and thrust forces generated over each stiffness actuator on the wing membrane, e.g., the E_n actuators described in Section 7.2, showed that the differences in the rigid and flexible wing lift and thrust phase averages (see Fig. 47) were due to force generation differences at localized sections of the wing planform during certain parts of the flapping cycle. In terms of thrust generation differences, the time from $t = \frac{1}{8}$ to $\frac{3}{8}$ of the total flapping cycle proved critical. During this period, the wingtips of the flexible wing showed dramatically less negative thrust (i.e., drag) production than the wingtips of the rigid wing. The lift generation during this time was approximately equal for both wings. For lift generation, the critical period was from $t = \frac{1}{2}$ to $\frac{5}{8}$ of the flapping cycle. In this short duration, the mid-span region of the rigid wing generates a larger negative lift force than the corresponding areas of the flexible wing. This led to the differential in the negative lift peaks observed in the

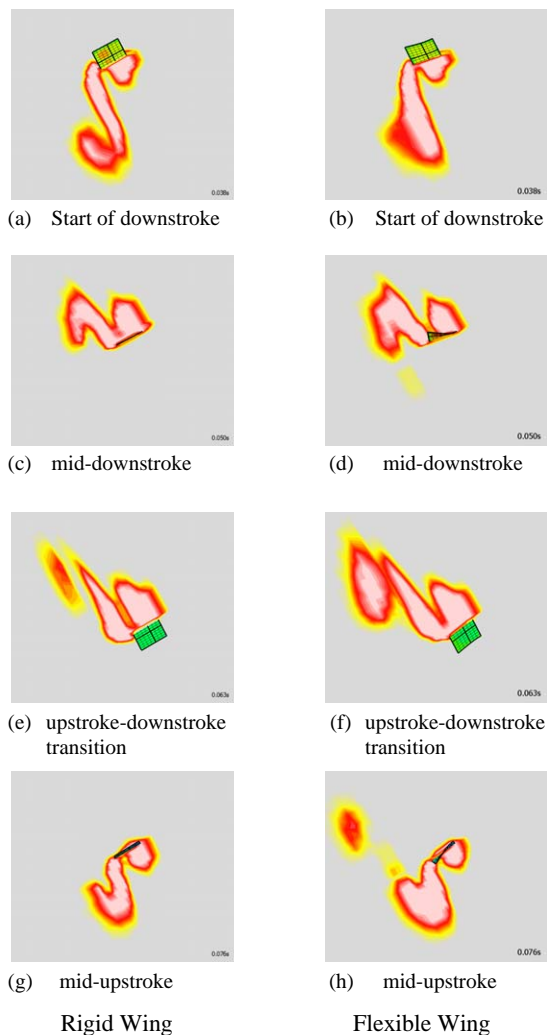


Fig. 48. Vorticity evolution at mid-span for rigid and flexible wings.

phase average measurements. The thrust forces were nearly equal during the same time period. It appeared then that the difference in the phase average thrust curves occur at the wingtips during the early downstroke and that the disparity in lift arises from the mid-span portion of the wing on the upstroke. Now that the areas of interest were located, a more detailed analysis of the near field flow at those locations was possible.

The thrust investigation started with force maps of the wings, as shown in Fig. 49, which details the difference

in lift and thrust forces between the upper and lower wing surfaces, i.e., the net lift and thrust forces. The lift force map is shown above the thrust map for each wing. From Fig. 49 it becomes apparent that while the lift forces distributions are quite similar for the two wings, the net thrust forces near the wingtips differ dramatically, with the base wing exhibiting much high negative thrust patches.

Fig. 50 examines the vorticity near the wingtip for both wings at $t = \frac{1}{8}$ of the total flapping cycle. The

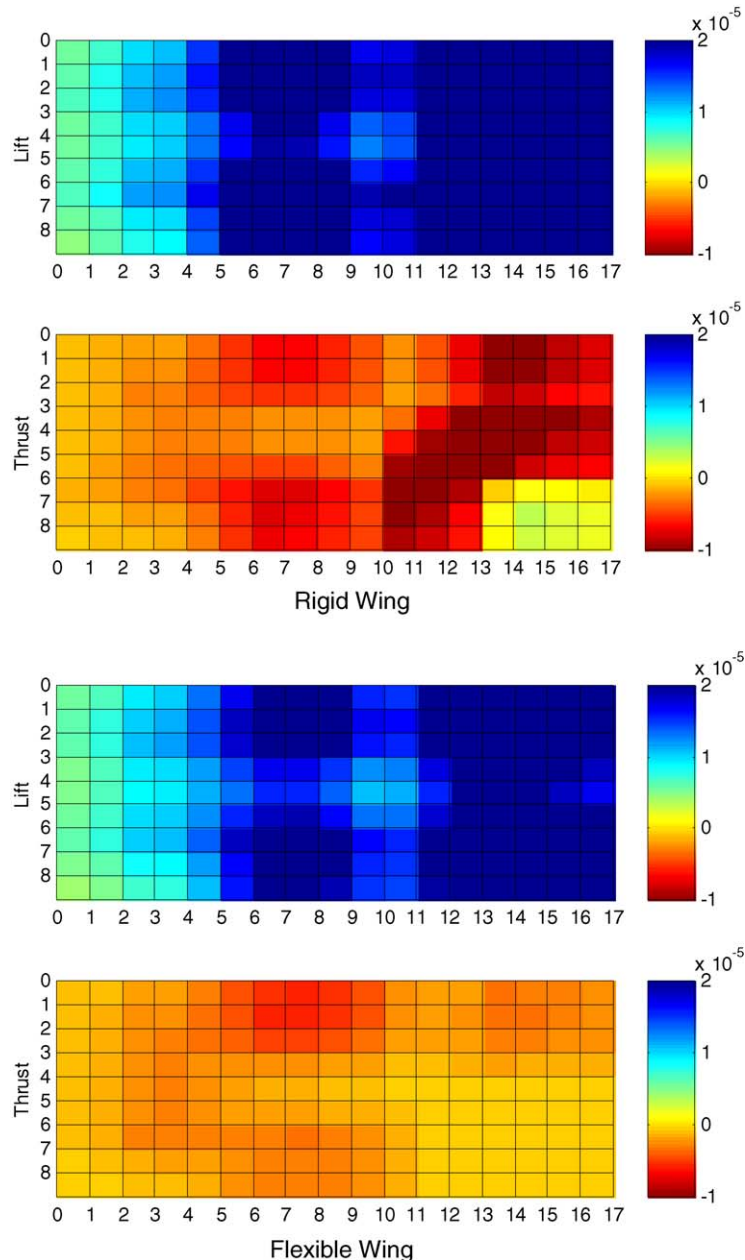


Fig. 49. Net lift and thrust force map of rigid and flexible wing at $\frac{1}{8}$ cycle.

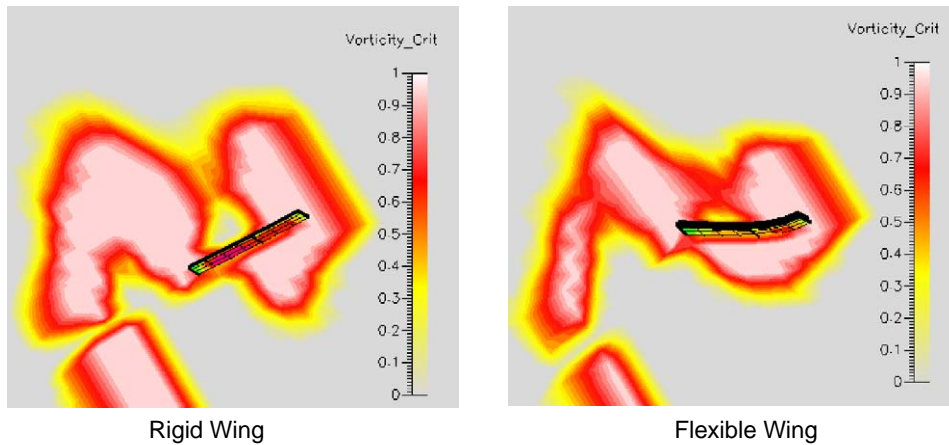


Fig. 50. Vorticity field near rigid and flexible wing at wingtips, $\frac{1}{8}$ cycle.

vorticity in the rigid case extends further at both the leading and trailing edges than for the optimal wing. The rigid wing vortex wake in particular is large in extent and sheds almost perpendicularly from the trailing edge of the wing. For the flexible wing, the trailing vortex wake tilts away from the trailing edge and is much smaller in size. The most noticeable difference, however, is that a relatively large low vorticity region sits above the trailing edge of rigid wing while this region is much smaller than for the flexible wing. The changes in vorticity, however, were not easily related to changes in the forces produced by the wing and the parameters governing force generation. As will be discussed later, *wing deformation and tilting of the total force vector* are the keys to changes in the lift and thrust generation.

Turning to the lift differences, Fig. 51 maps the net lift and thrust forces of the rigid and flexible wings at $t = \frac{5}{8}$ of the flapping period, i.e., immediately after the turn from downstroke to upstroke. Again, the rigid wing displays more extreme net forces than the flexible wing. Near the mid-span of the wing notice that the flexible wing creates less negative lift than the rigid wing. Physically, what happened is that areas of positive pressure atop the wing and of negative pressure below the wing seem reduced in size for the flexible wing compared to the rigid wing. Since negative pressure underneath the wing exerts a downward pull, the larger the negative pressure area, the larger the negative lift force. The positive pressure atop the wing also forces the wing in the downward direction and increases the negative lift. The sum of these two pressures across the membrane causes the negative lift peak seen in the phase average during the upstroke.

The physical phenomena causing a downward suction on the wing is the unsteady leading edge vortex that forms under the wing on the upstroke. Fig. 52 shows the vorticity field near the mid-span of both wings. Examining the vorticity field, there exists slight differ-

ences in the size of the two leading edge vortices underneath the wing and more substantial changes of the vorticity above the wing. Again, however, the changes in the vorticity field do not easily correlate to changes in the physical forces nor to an understanding of why the flexible and rigid wings vary in performance during the upstroke.

Understanding the physical mechanism behind the changes in force generation involves examining the changes in wing curvature between the rigid and flexible wings. The curvature on a wing bends the streamlines around the wing, causing differences in pressure gradients and hence lift and thrust effects. Variation in curvature will also tilt the total force vector and thereby resize the magnitude of the lift and thrust vector components, as shown in Fig. 53. For the rigid wing, a force near the wingtip is oriented at an angle θ_r with respect to the normal axes. A flexible wing, however, will cause the total force vector to tilt to a different angle, θ_f , and therefore change the drag and lift components in a favorable manner.

To validate this relation between wing curvature and rotation of the total force vector, the total force vector generated by each stiffness actuator for both wings was calculated. Fig. 54 plots the direction of the total force vector at each actuator location for each wing at $\frac{1}{8}$ and $\frac{5}{8}$ of the total flapping cycle, i.e., at the same time instants as for Figs. 49 and 51. The actuator location corresponds to the set of actuators denoted by E_n (see Fig. 43), such that Actuator 1 is E_1 , Actuator 2 is E_2 , etc. Hence, Actuators 1–3 are located at the leading edge, starting from the wing root (Actuator 1) and moving to the wingtip (Actuator 3). Actuators 4–6 are found at the trailing edge, starting near the wing root and ending at the wingtip.

Fig. 54 clearly shows that for the flexible wing, the direction of the total force vector changes as one moves from the chord to the wingtip region, while the direction

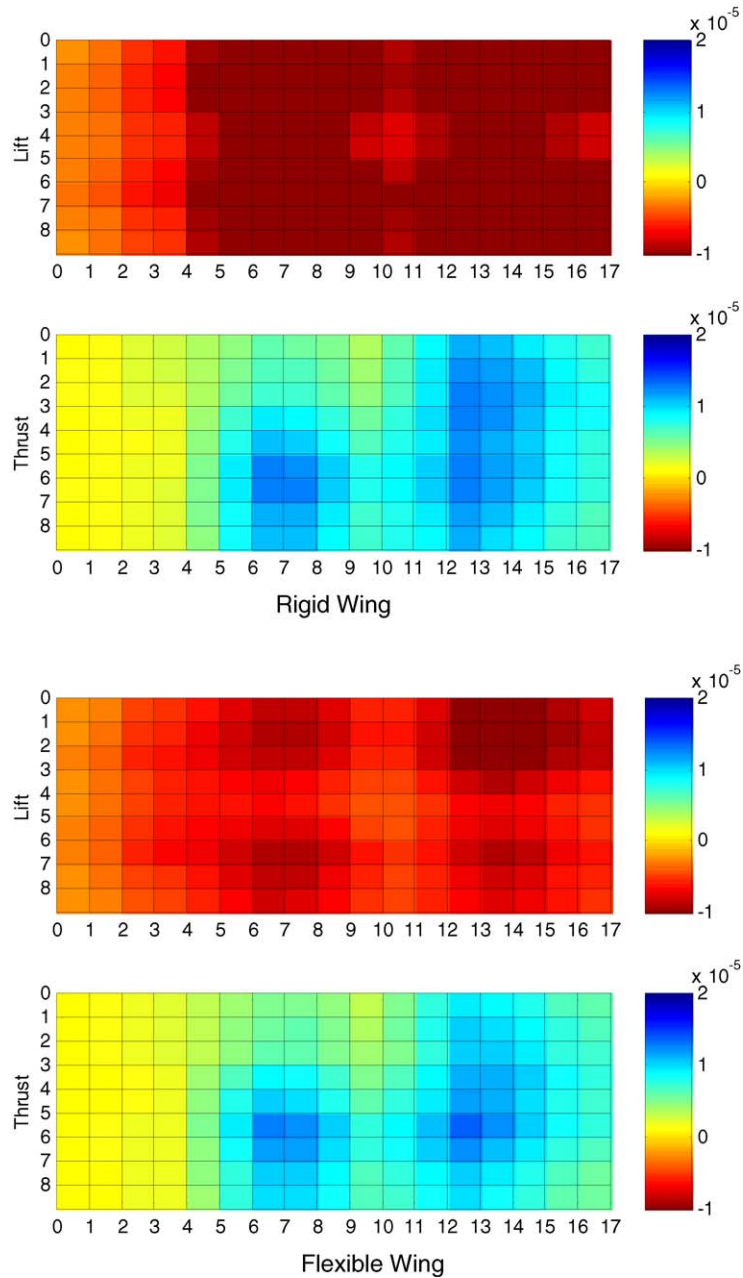


Fig. 51. Net lift and thrust force map of rigid and flexible wing at $\frac{5}{8}$ cycle.

remains nearly constant at -30° for the rigid case. As noted previously, this causes the lift and thrust components to change and indeed, the changes are favorable during the downstroke and upstroke. For example, at $t = \frac{1}{8}$ of the flapping cycle the thrust and lift of the flexible wing at the wingtip actuator location (Actuator 6) are 1.79×10^{-4} and 0.0163 N, respectively. At the same instant in time, the rigid wing thrust and lift are -0.0123 and 0.0223 N, respectively. Favorable

rotation also occurs at $t = \frac{5}{8}$ of the flapping cycle. At this time during the upstroke, the flexible wing displays a thrust and lift magnitude of 0.0134 and -0.008 N, respectively, while the rigid wing has a thrust and lift value of 0.0133 and -0.0021 N.

The correlation of the change in direction of the total force vector and the deflection of the wing can be verified. First, the change in direction is easily computed from the difference in angular orientation of the two

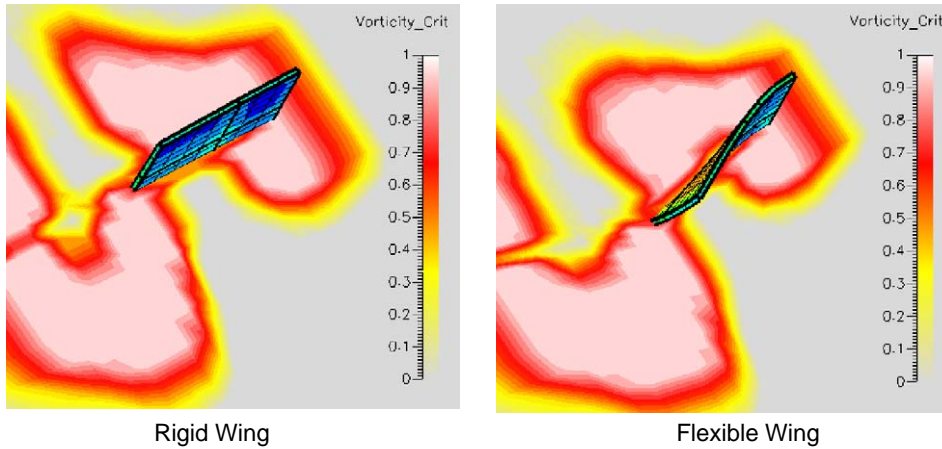


Fig. 52. Vorticity field at mid-span of rigid and flexible wing at $\frac{3}{8}$ cycle.

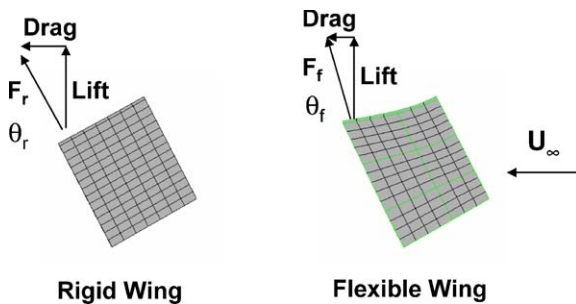


Fig. 53. Depiction of curvature changing lift and thrust vector components.

vectors, $\theta_f - \theta_r$. Then the deflection (in degrees) from the mean chordline for the flexible wing can be measured. This deflection equals the deformation change from the rigid wing since it exhibits very little change from the chordline due to its rigidity.

Fig. 55 graphs the correlation of the total force vector direction at each actuator location and the corresponding mean deflection from the chordline for both time points described previously. There obviously exists a strong correlation between the change in force vector direction and the mean wing deflection at each actuator location. The conclusion, therefore, is that curvature of the flexible wing caused a rotation of the force vector such that the detrimental components to thrust and lift were minimized during the flapping cycle. Physically, curvature caused changes in the streamlines around the wing that favorably impacted the pressure gradients responsible for lift and thrust.

7.4. Mechanical power

In the computational model, the motion of the leading edge and chord were prescribed to be a sinusoidal

motion in time, i.e., the velocity of those edges were predetermined, and thus the power input into the system was fixed. Given this condition, one measure of comparison between two different wings is to determine the mechanical power produced by each wing at the same baseline. For flapping flight, it is not as easy to separate lift and thrust as it is for conventional fixed wing aircraft. To determine equal baselines from which to measure the mechanical power production, one can fix the lift and from that calculate the thrust and forward velocity corresponding to that particular lift requirement. Once the thrust and flight speed are found, then it is a simple matter to compute the mechanical power and determine which wing more efficiently converts the input power into work.

The previous section examined the physical mechanisms behind the performance gains measured after using the Gur Game controller to find an optimal stiffness distribution. To calculate the mechanical power curve requires running the simulation over a range of flow speeds and computing the total lift and thrust generated over one flapping cycle. Fig. 56 shows the computed average lift and thrust produced by each rectangular wing over a set of velocities ranging from 0.7 to 4.7 m/s.

Examining Fig. 56, it is clear that the flexible wing outperforms the rigid wing in thrust with a fairly constant thrust differential over the entire speed range. At higher speeds, i.e., $U > 3.5$ m/s, the rigid wing creates more lift than the flexible wing, while the situation reverses for speeds below 3.5 m/s. As the flow transitioned from unsteady to quasi-steady, the flexible wing cannot maintain a performance advantage over the rigid wing, as seen at $U = 3.5$ m/s, which corresponded to $J = 1.2$. Based on these curves, a regression was performed and fitting parameters for each lift and thrust curve were extrapolated. From these regressions, average wing performance was calculated for both faster and slower flow speeds.

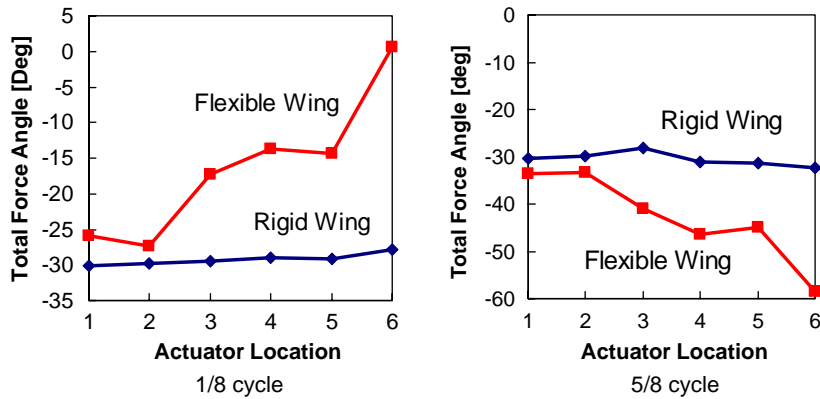


Fig. 54. Direction of total force vectors at snapshots during the flapping cycle.

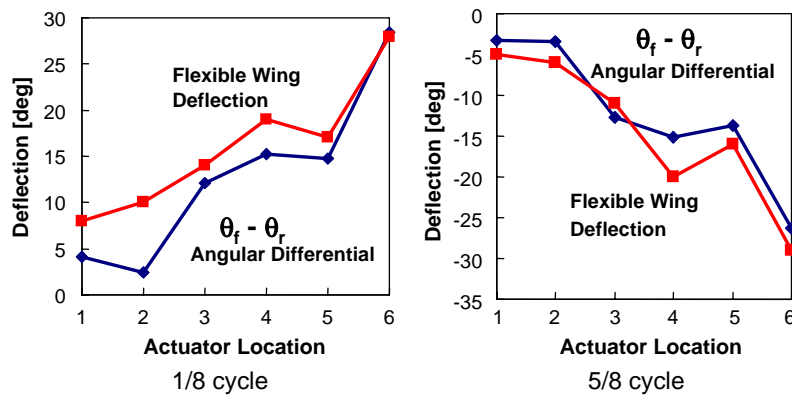


Fig. 55. Correlation of total force vector direction and wing deflection.

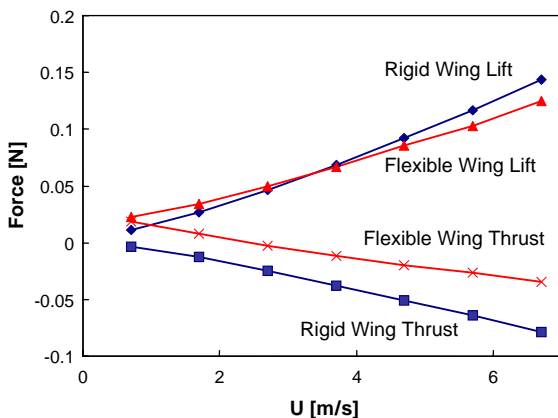


Fig. 56. Rigid and flexible wing lift and thrust as function of velocity.

The definition of mechanical power in aerodynamics is

$$P_{\text{mech}} = TU, \quad (26)$$

where T is thrust and U is flow velocity, respectively. For a fair comparison, the lift for each wing was equalized and the corresponding thrust and flow speeds, i.e., the corresponding mechanical power, were computed from the regressions. Fig. 57 compares the power performance based on this equal lift constraint.

Fig. 57 clearly shows the flexible wing producing more mechanical power than the rigid wing. The advantage in mechanical power that the flexible wing enjoys means that when the two wings carry the same payload, the flexible wing has excess power and therefore it can either accelerate, perform maneuvers, or simply extend its range by reducing its power consumption, while the rigid wing has no spare power to match the flexible wing performance. Also, note that peak power creation is near $U = 1.5$ m/s, which is where the advance ratio is well into the unsteady regime with $J = 0.6$ and falls to zero near where $J = 1$, i.e., in the transition between the unsteady and quasi-steady regimes. This supports the idea that a flexible wing is works best when unsteady aerodynamic mechanisms can be exploited.

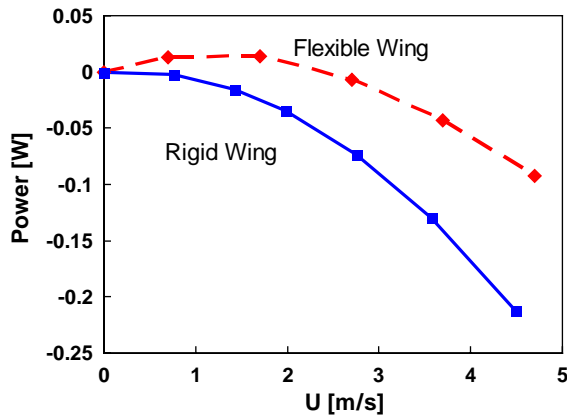


Fig. 57. Power comparison between rigid and flexible CFD wings.

7.5. Summary of the simulation project

After validating the three dimensional, unsteady, and fully coupled aeroelastic simulation model against experimental fully flexible MEMS wing test data, the next logical step was applying the Gur Game algorithm to control and optimize the wing stiffness. The optimization proved successful and converged upon a wing that performed considerably better than the original wing for different wing planforms. For greater generality, reduced computational time, and ease of modeling, the majority of the analysis used a plain rectangular wing.

Several key points surfaced during the analysis. Notably, wings must exhibit a large degree of flexibility to achieve positive thrust and lift. A rigid or stiff wing simply is not a viable design. This correlates well with knowledge gained experimentally. The optimized wings also mimicked the experimental wing designs in that the wingtips should be stiffer than the membrane for good performance. This is a somewhat unexpected result, as the wing planforms were very different between the vast majority of wings tested in the wind tunnel and the computational model.

Another surprising result was that the optimal wings gained their advantage not from increasing the positive force peaks, but instead by reducing the drag on the downstroke and the negative lift of the upstroke. The physical causes of this were that the curvature of the flexible wing induced changes in the streamlines surrounding the wing and altered the pressure gradients in a positive manner. The effect of curvature on the force vectors is to tilt them in a favorable manner, such that the negative thrust and negative lift components were reduced for the flexible wing compared to the rigid wing.

8. Concluding remarks

This article reviewed the unsteady aerodynamics, aeroelastic phenomena, and several flow control strategies for flapping wing flight, with an eye toward application of these theories to raising the performance of MAVs. Simple scaling arguments demonstrated that small and slow flying MAVs will operate in a fully unsteady flow regime and, as a result, quasi-steady aerodynamic analysis is not appropriate. Furthermore, the presence of highly flexible wings in an unsteady flow created a difficult aeroelastic analysis, but one that must be considered, as the flow–structure interaction proved important in determining overall lift and thrust.

Past researchers have uncovered a number of unsteady flow mechanisms that enhanced lift and thrust generation for flapping wings. These include “clap and fling”, rotational lift and wake capture, and, most prominently, the unsteady leading edge vortex. The unsteady leading edge vortex and the stiffness distribution of the wing were shown to dominant the lift and thrust production. In particular, the growth of a stable separation bubble atop the wing during the downstroke appears to be the mechanism to explain the high unsteady lift coefficients found for flapping fliers in forward flight. The stiffness distribution also plays major roles in both lift and thrust generation. A wing that is stiff in the spanwise direction near the leading edge is advantageous in terms of lift in the unsteady flow domain, while one that is spanwise flexible causes a sharp drop in lift for unsteady conditions. In terms of thrust, experiments indicated that the wing stiffness, particularly near the trailing edge, determined the final thrust output.

Following the aerodynamic analysis, a literature review revealed a large body of work on both passive and active flow control methods of separated flows. Control of the vortex atop delta wings, of the dynamic stall on rotating airfoils, and of flutter indicates that a large degree of control authority in unsteady flow is possible. The majority of this work was done for open loop systems. These open loop control cases were relevant to MAV flight since once the flow separates at the leading edge, the physical phenomena involved (vortex generation and convection) are largely Reynolds number independent. Hence, perhaps the same lessons from these large-scale cases can be applied to the mesoscale MAV wing.

Although a number of closed loop feedback control algorithms were investigated in the literature, the highly nonlinear nature of the system precluded the use of linear control schemes. Instead, attention focused on fuzzy controllers, such as genetic algorithms and neural networks, and their ability to predict and control separated flows. The Gur Game, an algorithm for self-optimization and self-organization for distributed

nonlinear systems, was also presented. The Gur Game proved itself capable of significantly altering the aerodynamic performance of the wings using simple variation of the drive signal in wind tunnel tests.

Finally, a description of an unsteady, three dimensional, and fully coupled aeroelastic computational fluid dynamic model with an integrated distributed feedback control algorithm to optimize wing membrane flexibility was presented. The results of the model demonstrated that flexible membranes improved lift and thrust performance not by maximizing the positive force peaks, but rather by minimizing the negative peaks. Further, these performance gains arose from localized areas of the wing during very short time periods of the overall flapping cycle. The physical mechanism for these gains was that wing deformation due to increased flexibility caused a favorable tilting of the overall force vector, thereby reducing the negative force components.

Clearly there remains a vast amount of work to be carried out in the field of flexible flapping wing flight and its control. More analytic research in the underlying aeroelastic problem of flexible wings interacting with vortex flows would provide valuable insight and design guidance for future MAVs. Advanced computational models using the full Navier–Stokes equations coupled with a FEM would greatly aid in understanding the physical phenomena driving the instantaneous and time averaged lift and thrust forces. In the design, fabrication, and operations arena, new lightweight actuators and actuation systems to deal with unsteady vortex flows will likely prove invaluable in the control and optimization of MAV flight. Additionally, investigations of new control algorithms expressly created for nonlinear systems would benefit not only the MAV community but advanced aeronautic designs as well. We hope this article provides sufficient material to highlight the challenges and possibilities in MAV flight and will aid future designers and researchers in the field.

Acknowledgements

This project is supported by DARPA and the NSF Engineering Research Center at Caltech.

References

- [1] Dial KP. An inside look at how birds fly: experimental studies of the internal and external processes controlling flight. 1994 Report the Aerospace Profession, 38th Symposium Proceedings, The Beverly Hilton, Beverly Hills, CA, 1994.
- [2] Greenewalt CH. Dimensional relationships for flying animals. *Smithson Misc Collect* 1962;144:1–46.
- [3] Greenewalt CH. The flight of birds. *Trans Am Philos Soc* 1975;65:1–67.
- [4] Norberg UM. Vertebrate flight: mechanics, physiology, morphology, ecology, and evolution. New York: Springer; 1990.
- [5] Pennycuik CJ. Wingbeat frequency of birds in steady cruising flight: new data and improved predictions. *J Exp Biol* 1996;199:1613–8.
- [6] Pennycuik CJ. Actual and 'optimum' flight speeds: field data reassessed. *J Exp Biol* 1997;200:2355–61.
- [7] Weis-Fogh T, Jensen M. Biology and physics of locust flight, I–IV. *Philos Trans R Soc London Ser B* 1956;239:415–58.
- [8] Lighthill MJ. Mathematical biofluidynamics. Philadelphia, PA: Society for Industry and Applied Mathematics; 1975.
- [9] Rayner JMV. A vortex theory of animal flight. Part 1. The vortex wake of a hovering animal. *J Fluid Mech* 1979;4:697–730.
- [10] Rayner JMV. A vortex theory of animal flight. Part 2. The forward flight of birds. *J Fluid Mech* 1979;4:731–63.
- [11] Ellington CP. The aerodynamics of hovering insect flight IV. Aerodynamic mechanisms. *Philos Trans R Soc London Ser B* 1984;305:79–113.
- [12] Ellington CP. The aerodynamics of hovering insect flight V. A vortex theory. *Phil Trans R Soc Lond Ser B* 1984;305:115–44.
- [13] Dickinson MH, Lehmann FO, Sane SP. Wing rotation and the basis of insect flight. *Science* 1999;284:1954–60.
- [14] Spedding GR, Lissaman PBS. Technical aspects of microscale flight systems. *J Exp Biol* 1998;29:458–68.
- [15] Spedding GR. The aerodynamics of flight. *Adv Comp Env Physiol* 1992;11:51–111.
- [16] Tobalske BW, Dial KP. Flight kinematics of black-billed magpies and pigeons over a wide range of speeds. *J Exp Biol* 1996;199:263–80.
- [17] Nachtigall W. Die kinematik der Schlagflügelbewegungen von Dipteren methodische und analytische Grundlagen zur Biophysik des Insektenflugs. *Z Vgl Physiol* 1966;22:155–211.
- [18] Nachtigall W. *Insects in flight*. New York: McGraw-Hill; 1974.
- [19] Rayner JMV. Mechanical and ecological constraints on flight evolution. In: Hecht MK, Ostrom JH, Viohl G, Wellenhofer P, editors. *The beginnings of birds*. Eichstätt: Jura Museum; 1985.
- [20] Rayner JMV. Vertebrate flapping flight mechanics and aerodynamics, and the evolution of flight in bats. *Biona Rep* 1985;5:27–74.
- [21] Norberg UM. Evolution of vertebrate flight: an aerodynamic model for the transition from gliding to active flight. *Am Nat* 1985;126:303–27.
- [22] Pennycuik CJ. On the reconstruction of Pterosaurs and their manner of flight, with notes on vortex wakes. *Biol Rev* 1988;63:299–331.
- [23] Azuma A, Azuma S, Watanabe I, Furuta T. Flight mechanics of a dragonfly. *J Exp Biol* 1985;116:79–107.
- [24] Azuma A, Watanabe T. Flight performance of a dragonfly. *J Exp Biol* 1988;137:221–52.
- [25] Wakeling JM, Ellington CP. Dragonfly flight I. Gliding flight and steady-state aerodynamics. *J Exp Biol* 1997;200:543–56.

- [26] Wakeling JM, Ellington CP. Dragonfly flight II. Velocities, accelerations, and kinematics of flapping flight. *J Exp Biol* 1997;200:557–82.
- [27] Wakeling JM, Ellington CP. Dragonfly flight III. Quasi-steady lift and power requirements. *J Exp Biol* 1997;200:583–600.
- [28] Van Den Berg C, Rayner JMV. The moment of inertia of bird wings and the inertial power requirements for flapping flight. *J Exp Biol* 1995;198:1644–64.
- [29] Rayner JMV. Estimate power curves of flying vertebrates. *J Exp Biol* 1999;202:3449–61.
- [30] Rayner JMV. Mathematical modeling of the avian flight power curve. *Math Meth Appl Sci* 2001;24:1485–514.
- [31] Dickinson MH, Gotz KG. Unsteady aerodynamic performance of model wings at low Reynolds numbers. *J Exp Biol* 1993;174:45–64.
- [32] Ellington CP, Van Den Berg C, Willmott AP, Thomas ALR. Leading-edge vortices in insect flight. *Nature* 1996;384:626–30.
- [33] Maxworthy T. Experiments on the Weis-Fogh mechanism of lift generation by insects in hovering flight. Part 1. Dynamics of the ‘fling’. *J Fluid Mech* 1979;93:47–63.
- [34] Van Den Berg C, Ellington CP. The three-dimensional leading-edge vortex of a hovering model hawkmoth. *Philos Trans R Soc London Ser B* 1997;353:329–40.
- [35] Smith MJC. Simulating moth wing aerodynamics: towards the development of flapping-wing technology. *AIAA J* 1996;34:1348–55.
- [36] Shyy W, Jenkins DA, Smith RW. Study of adaptive shape airfoils at low Reynolds number in oscillatory flow. *AIAA J* 1997;35:1545–8.
- [37] Levin O, Shyy W. Optimization of a low Reynolds number airfoil with flexible membrane. *Comput Model Eng Sci* 2001;2:523–36.
- [38] Ramamurti R, Sandberg WC. A three-dimensional computational study of the aerodynamic mechanisms of insect flight. *J Exp Biol* 2002;205:1507–18.
- [39] Sun M, Tang J. Unsteady aerodynamic force generation by a model fruit fly wing in flapping motion. *J Exp Biol* 2002;205:55–70.
- [40] Wang ZJ. Vortex shedding and frequency selection in flapping flight. *J Fluid Mech* 2000;410:323–41.
- [41] Liu H, Ellington CP, Kawachi K, Van den Berg C, Willmott AP. A computational fluid dynamic study of hawkmoth hovering. *J Exp Biol* 1998;201:461–77.
- [42] Shyy W, Berg M, Ljungqvist D. Flapping and flexible wings for biological and micro air vehicles. *Prog Aerosp Sci* 1999;35:455–506.
- [43] Tennekes H. The simple science of flight (from insects to jumbo jets). Boston, MA: MIT Press; 1996.
- [44] McCormick BW. Aerodynamics, aeronautics, and flight mechanics. New York: Wiley; 1979.
- [45] Pennycuik CJ. Mechanical constraints on the evolution of flight. *Mem Cal Sci* 1986;8:83–98.
- [46] Pennycuik CJ. The mechanics of bird migration. *Ibis* 1969;111:525–56.
- [47] Azuma A. The biokinetics of flying and swimming. Tokyo: Springer; 1992.
- [48] Pennycuik CJ. Bird flight performance: a practical calculation manual. New York: Oxford University Press; 1989.
- [49] Betteridge DS, Archer RD. A study of mechanics of flapping flight. *Aeronaut J* 1974;25:129.
- [50] Archer RD, Sapuppo J, Betteridge DS. Propulsion characteristics of flapping wings. *Aeronaut J* 1979;83:355–71.
- [51] Ellington CP. The aerodynamics of hovering insect flight I. The quasi-steady analysis. *Philos Trans R Soc London Ser B* 1984;305:1–15.
- [52] Sane SP, Dickinson MH. The control of flight force by a flapping wing: lift and drag production. *J Exp Biol* 2001;204:2607–26.
- [53] Weis-Fogh T. Quick estimates of flight fitness in hovering animals, including novel mechanisms for lift production. *J Exp Biol* 1973;59:169–230.
- [54] Ellington CP. The novel aerodynamics of insect flight: application to micro-air vehicles. *J Exp Biol* 1999;202:3439–48.
- [55] Maxworthy T. Experiments on the Weis-Fogh mechanism of lift generation by insects in hovering flight. *J Fluid Mech* 1979;93:47–63.
- [56] Vest MS, Katz J. Unsteady aerodynamic model of flapping wings. *AIAA J* 1996;34:1435–40.
- [57] Dickinson MH, Lehmann FO, Gotz KG. The active control of wing rotation by *Drosophila*. *J Exp Biol* 1993;182:173–89.
- [58] Liu H, Kawachi K. A numerical study of insect flight. *J Comp Phys* 1998;146:124–56.
- [59] Ho S, Nassef H, Pornsin-Sirirak TN, Tai YC, Ho CM. Flight dynamics of small vehicles. Proceedings of the 23rd International Congress on Aerospace Sciences, Toronto, Canada, September 9–12, 2002.
- [60] Pornsin-Sirirak TN, Lee SW, Nassef H, Grasmeyer J, Tai YC, Ho CM, Keenon M. MEMS wing technology for a battery-powered ornithopter. The 13th IEEE International MEMS Conference (MEMS '00), Miyazaki, Japan, January 23–27, 2000.
- [61] Pornsin-Sirirak TN, Nassef H, Tai YC, Ho CM. Flexible parylene actuator for micro adaptive flow control. The 14th IEEE International MEMS Conference (MEMS '01), Interlaken, Switzerland, January 21–25, 2001.
- [62] Pornsin-Sirirak TN, Liger M, Tai YC, Ho S, Ho CM. Flexible parylene-valved skin for adaptive flow control. The 15th IEEE International MEMS Conference (MEMS '02), Las Vegas, NV, January 20–24, 2002.
- [63] Bennet AG, Obye RC, Jeglum PM. Ornithopter aerodynamic experiments. In: Wu TY-T, Brokaw CJ, Brennen C, editors. Swimming and flying in nature, vol. 2. New York: Plenum Press; 1975.
- [64] Smith MJC, Wilkin PJ, Williams MH. The advantages of an unsteady panel method in modeling the aerodynamic forces on rigid flapping wings. *J Exp Biol* 1996;199:1073–83.
- [65] Smith MJC. Simulating flapping wings using an aerodynamic panel method. PhD thesis, Purdue University, 1995.
- [66] Shyy W, Kleverbring F, Nilsson M, Sloan J, Carroll B, Fuentes C. A study of rigid and flexible low Reynolds number airfoils. *J Aircraft* 1999;36:523–9.
- [67] Vasquez RJ. The automated skeletal and muscular mechanisms of the avian wing. *Zoomorphology* 1994;114:59–71.

- [68] Maybury WJ, Rayner JMV. The avian tail reduces body parasitic drag by controlling flow separation and vortex shedding. *Philos Trans R Soc London Ser B* 2001; 268:1405–10.
- [69] Rayner JMV, Maybury WJ, Couldrick LB. Lift generation by the avian tail. *Proc R Soc Biol Sci B* 2001; 268:1443–8.
- [70] Bechert DW, Bruse M, Hage W, Meyer R. Biological surfaces and their technological application-laboratory and flight experiments on drag reduction and separation control. AIAA Paper No 97-1960, 1997.
- [71] Kockler R, Wedekind F, Gesser R, Nachtigall W. Aspekte zur bionischen übertragung einiger aerodynamischer strukturen des vogelflügels. In: Blickhan R, Wisse A, Nachtigall W, editors. *Motion systems Biona Report* Gustav Fisher Verlag. Stuttgart, Germany 1998; 13:201–2.
- [72] Muller W, Patone G. Air transmissivity of feathers. *J Exp Biol* 1998;201:2591–9.
- [73] Drovetski SV. Influence of the trailing edge notch on flight performance of Galliforms. *Auk* 1996;113: 802–10.
- [74] Brown RHJ. The forward flight of birds. *Biol Rev* 1963;38:460–89.
- [75] Gu W, Robinson O, Rockwell D. Control of vortices on a delta wing by leading-edge injection. *AIAA J* 1992;31: 1177–86.
- [76] McCormick S, Gursul I. Effect of shear-layer control on leading-edge vortices. *J Aircraft* 1996;33:1087–93.
- [77] Badran B, McCormick S, Gursul I. Control of leading-edge vortices with suction. *AIAA J* 1997;35: 163–5.
- [78] Lee GB. The control of a delta-wing aircraft by micro machined sensors, actuators. PhD thesis, University of California, Los Angeles, CA, 1998.
- [79] Huang PH, Folk C, Silva C, Christensen B, Chen Y, Ho CM, Jiang F, Grosjean C, Tai YC, Lee GB, Chen M, Newbern S. Applications of MEMS devices to delta wing aircraft: from concept development to transonic flight test. AIAA Paper No. 2001-0124, 2001.
- [80] Shih C, Ding Z. Trailing-edge jet control of leading edge vortices of a delta wing. *AIAA J* 1996;34: 1447–57.
- [81] Vorobieff PV, Rockwell DO. Multiple actuator control of vortex breakdown on a pitching delta wing. *AIAA J* 1996;34:2184–6.
- [82] Vorobieff PV, Rockwell DO. Vortex breakdown on pitching delta wing: control of intermittent trailing-edge blowing. *AIAA J* 1998;36:585–9.
- [83] McCroskey WJ, McAlister KW, Carr LW. Dynamic stall experiments on oscillating airfoils. *AIAA J* 1976;14: 57–63.
- [84] Alrefai M, Acharya M. Controlled leading-edge suction for management of unsteady separation over pitching airfoils. *AIAA J* 1996;34:2327–36.
- [85] Carr LW, McAlister KW. The effect of a leading-edge slat on the dynamic stall of an oscillating airfoil. AIAA Paper No. 83-2533, 1983.
- [86] Yu Y, Lee S, McAlister KW, Tung C, Wang CM. Dynamic stall control for advanced rotorcraft application. *AIAA J* 1995;33:289–96.
- [87] Alexander H. Active control of dynamic stall. PhD thesis, University of California, Los Angeles, CA, 1998.
- [88] Prophet, EM. Controlling dynamic stall using multiple actuators. MS thesis, University of California, Los Angeles, CA, 2000.
- [89] Bisplinghoff RL, Ashley H, Halfman RL. *Aeroelasticity*. New York: Dover Publications Inc; 1996.
- [90] Lin CY, Crawley EF, Heeg J. Open- and closed-loop results of a strain-actuated active aeroelastic wing. *J Aircraft* 1996;33:987–94.
- [91] Madou M. *Fundamentals of microfabrication*. New York, NY: CRC Press; 1997.
- [92] Kovacs G. *Micromachined transducers sourcebook*. New York, NY: WCB/McGraw Hill; 1998.
- [93] Ho CM, Tai YC. Review: MEMS and its applications for flow control. *J Fluid Eng* 1996;118:437–47.
- [94] Ho CM, Tai YC. Micro-electro-mechanical systems (MEMS) and fluid flows. *Ann Rev Fluid Mech* 1998; 30:579–612.
- [95] Fukang J, Lee GB, Tai YC, Ho CM. A flexible micromachine-based shear stress array and its application to separation-point detection. *Sensors Actuators A* 2000; 79:194–203.
- [96] Liger M, Pornsin-Sirirak N, Tai YC, Ho S, Ho CM. Large-area electrostatic-valved skins for adaptive flow control on ornithopter wings. *Solid State Sensors, Actuator, and Microsystems Workshop*, Hilton Head Island, South Carolina, 2002, p. 247–50.
- [97] Pornsin-Sirirak N. *Parylene MEMS technology*. PhD thesis, California Institute of Technology, 2002.
- [98] Edwards JW, Breakwell JV, Bryson Jr AE. Active flutter control using generalized unsteady aerodynamic theory. *J Guidance Control* 1977;1:32–40.
- [99] Newsom JR. Control law synthesis for active flutter suppression using optimal control theory. *J Guidance Control* 1979;2:388–94.
- [100] Mahesh JK, Stone CR, Garrard WL, Dunn HJ. Control law synthesis for flutter suppression using linear quadratic Gaussian theory. *J Guidance Control* 1981;4: 415–22.
- [101] Mukhopadhyay V. Flutter suppression control law design and testing for the active flexible wing. *J Aircraft* 1995;32:45–51.
- [102] Lazarus KB, Crawley EF, Lin CY. Multivariable active lifting surface control using strain actuation: analytical and experimental results. *J Aircraft* 1997;34: 313–21.
- [103] Lutton JA, Mook DT. Numerical simulations of flutter and its suppression by active control. *AIAA J* 1993;31:2312–9.
- [104] Frampton KD, Clark RL, Dowell EH. Active control of panel flutter with piezoelectric transducers. *J Aircraft* 1996;33:768–74.
- [105] Gursul I, Srinivas S, Batta G. Active control of vortex breakdown over a delta wing. *AIAA J* 1995;33: 1743–5.
- [106] Milano M, et al. Evolving strategies for active flow control. In: 2000 IEEE Congress on Evolutionary Computation, La Jolla CA, 2000.
- [107] Milano M, Koumoutsakos P. A clustering genetic algorithm for actuator optimization in flow control.

- In: The Second NASA/DoD Workshop on Evolvable Hardware, Palo Alto, CA, 2000.
- [108] Faller WE, Schreck SJ, Luttgies MW. Neural network prediction and control of three-dimensional unsteady separated flowfields. *J Aircraft* 1995;32: 1213–20.
 - [109] Tung B, Kleinrock L. Using finite-state automata to produce self-optimization and self-control. *IEEE Trans Parallel Distributed Syst* 1996;7:439–48.
 - [110] Tung B. Distributed control using finite state automata. PhD thesis, University of California, Los Angeles, 1994.
 - [111] Tsetlin ML. Automation theory and modeling of biological systems, vol. 102. New York, NY: Academic Press; 1973.
 - [112] Ho, S. Unsteady aerodynamics and adaptive flow control of micro air vehicles. PhD thesis, University of California, Los Angeles, 2003.